HHS Public Access

Author manuscript

Nat Biotechnol. Author manuscript; available in PMC 2022 April 04.

Published in final edited form as:

Nat Biotechnol. 2022 March ; 40(3): 364–373. doi:10.1038/s41587-021-01041-z.

Highly-multiplexed volumetric mapping with Raman dye imaging and tissue clearing

Lixue Shi[#1], **Mian Wei**[#1], **Yupeng Miao**[1], **Naixin Qian**[1], **Lingyan Shi**[1,‡], **Ruth A. Singer**[2,§], **Richard K. P. Benninger**[3], **Wei Min**[1,4,*]

[1]Department of Chemistry, Columbia University, New York, NY, USA.

[2]Graduate Program in Cellular, Molecular and Biomedical Studies, Columbia University Medical Center, New York, NY, USA.

[3]Department of Bioengineering, University of Colorado Anschutz Medical Campus, Aurora, CO, US

[4]Kavli Institute for Brain Science, Columbia University, New York, NY, USA.

[#] These authors contributed equally to this work.

Abstract

Mapping the localization of multiple proteins in their native 3D context would be useful across many areas of biomedicine, but multiplexed fluorescence imaging has limited intrinsic multiplexing capability, and most methods for increasing multiplexing can only be applied to thin samples (<100 μm). Here we harness the narrow spectrum of Raman spectroscopy and introduce Raman Dye Imaging and Tissue Clearing (RADIANT), an optical method that is capable of imaging multiple targets in thick samples in one shot. We expanded the range of suitable bioorthogonal Raman dyes and developed a tissue clearing strategy for them (rDISCO). We applied RADIANT to image up to eleven targets in millimeter thick brain slices, extending the imaging depth 10–100 fold compared to prior multiplexed protein imagining methods. We showcased the utility of RADIANT in extracting systems information including region-specific correlation networks and their topology in cerebellum development. RADIANT will facilitate the exploration of the intricate 3D protein interactions in complex systems.

[*]Corresponding author: wm2256@columbia.edu.

[‡]Present address: Department of Bioengineering, University of California San Diego, La Jolla, CA, USA.

[§]Present address: Laboratory of Molecular Neuro-oncology, Rockefeller University, New York, NY, USA.

Author contributions

Lixue Shi and M.W. developed the protocols, performed the experiments and analyzed data; Y.M. performed MARS probe synthesis and characterization with the help of N.Q.; Lingyan Shi contributed to mouse sample preparation; R.A.S. and R.K.P.B. contributed to pancreas sample preparation; Lixue Shi, M.W. and W.M. conceived the concept and wrote the manuscript with input from all authors.

Competing interests

The authors declare no competing interests.

Code availability

The code used to analyze data are available from the corresponding author upon reasonable request.

Introduction

Biological systems consist of a large number of interacting components in their native three-dimensional (3D) environment. This theme recurs at nearly every length scale, ranging from protein networks, to organelles within cells, to various cell types within tissues, to synergistic tissues within functional organs, and reaching maximum complexity in the nervous system. Indeed, numerous highly diversified cell types exist and intermix in the central nervous system. For example, in the frontal cortex alone, recent methylome study identified at least 16 neuronal subtypes in mice and 21 neuronal subtypes in humans[1]. Moreover, individual neurons can extend in many directions and project over long distances[2]. Hence, mapping multiple proteins over a large volume is critical in understanding complex biological systems.

Fluorescence microscopy is the prevalent technique for protein imaging. However, due to fast electronic dephasing, fluorescence spectrum is too broad to spectrally resolve many targets at once, known as the “color barrier” (Fig. 1). As a result, typically no more than 5 targets can be simultaneously imaged (or 7 using specialized instrumentation and analysis[3,4]). To visualize a large number of targets at the same time, highly multiplexed protein imaging techniques have been developed. However, these methods are mostly confined to relatively thin samples (Fig. 1). Mass-spectrometry-based methods are inherently surface techniques[5,6]. Cyclic immunofluorescence performs multiple (often >10) rounds of labeling, antibody stripping (or photobleaching) and re-staining[7–10]. However, cyclic methods are extremely difficult to be applied to thick tissues due to several inherent limitations. First, multiple rounds of 3D immunostaining could take unpractically long time. 3–8 days is typically required for antibodies to penetrate into 1-mm-thick tissues (Supplementary Table 1), and hence 10 rounds of staining and de-staining will be prohibitively lengthy. Second, repeated tissue processing, especially volumetric antibody stripping and post-clearing re-staining, can cause accumulated antigen loss and fine structural damage[5]. CLARITY reported three cycles on 1-mm-thick tissue[11], but possibly with compromised structural and antigen integrity[12,13]. Third, 3D image co-registration and subsequent inference becomes much more difficult than the 2D counterpart due to non-linear volumetric histological changes among different cycles[5]. Owing to these limitations, despite recent innovations on engineering tissues[13–15], cyclic immunofluorescence has only been demonstrated in a relatively superficial depth (~100 μm) with a limited number of cycles even in the best case scenario. Thus, in spite of its perceived importance, highly multiplexed protein imaging in large 3D volume remains uncharted.

Our premise is that the above difficulties can be overcome if one can employ a one-shot optical method. To develop such technology, we harness advanced Raman microscopy. Owing to much narrower vibrational peaks (~10 cm^{-1}) compared to fluorescence (~500 cm^{-1}), Raman imaging can in principle break the fluorescence color barrier[16]. For example, Cy5, one of commonly used fluorescent dyes, shows a 50-nm (~700 cm^{-1}) FWHM in the fluorescence spectrum, but the Raman signature of its double bond in the fingerprint region is only 12 cm^{-1} in width[16]. Thus Raman spectroscopy poses a fundamental advantage for multiplexing in one shot. However, its sensitivity is generally far from ideal for imaging specific proteins inside cells[17]. Recently, by combining electronic pre-

resonance spectroscopy with stimulated Raman scattering (SRS) microscopy (i.e., epr-SRS), the Raman cross sections of electronically coupled vibrational modes in light-absorbing dyes can be enhanced by 10^{13} folds[16,18]. As a result of this drastic enhancement, we achieved nanomolar sensitivity of Raman-active dyes (such as those commercial far-red fluorescent dyes and specially-designed MARS probes with conjugated triple bonds[19]), and demonstrated epr-SRS imaging of specific proteins inside cells[16]. Hence the sensitivity issue of protein imaging by Raman microscopy is largely solved (Supplementary Note 1). However, as an optical technique, imaging depth of epr-SRS is still limited by the inevitable light scattering inside biological tissues. As a result, the epr-SRS imaging reported so far was performed only on thin tissue sections.

Thus we aim to generalize epr-SRS to large-scale volumetric imaging. Our inspiration comes from the recent success of tissue clearing technology, a powerful strategy to gain deep optical access inside tissues by homogenizing refractive indices[20,21]. However, the coupling of epr-SRS with tissue clearing can be easily hampered by the high-concentration chemicals inside refractive index matching solutions (RIMS), which could produce overwhelming Raman background interfering with the desired signature of Raman-active dyes. To explore this unknown paradigm, we adopted a systematic strategy to optimize the coupling between epr-SRS microscopy and tissue clearing. We started by examining the spectral compatibility of Raman-active dyes with tissue clearing protocols. The results suggested unsuitability of commercial dyes for this task, and prompted us to develop new bioorthogonal vibrational probes. These new probes allowed for immuno-eprSRS imaging of various protein targets in diverse tissue types under different sample preparations. Then we screened and compared common tissue clearing methods for volumetric epr-SRS imaging, and the obtained insights led to our optimization of rDISCO as a Raman-dye-tailored tissue clearing method. With the synergistic developments along both probes and tissue clearing, we achieved one-shot multiplexed imaging of more than 10 targets in millimeter-thick brain tissues, which extends the imaging depth of currently the best volumetric cyclic immunofluorescence results by 10 folds. We name this new method as Raman Dye Imaging and Tissue Clearing (RADIANT), which has unique advantages for thick tissues in that antibody staining and imaging can be performed for all targets in one shot, thereby circumventing the abovementioned limitations with cyclic immunofluorescence techniques. We further demonstrated its utility in extracting systems information including regional segmentation, spatial correlation, cellular composition, 3D distance and network topology during cerebellum development.

Results

Compatibility study of Raman dyes with tissue clearing

As tissue clearing is almost exclusively developed for fluorescence microscopy, we need to first study whether Raman-active dyes can be imaged after tissue clearing protocols. A potential pitfall, which is new for Raman microscopy but not for fluorescence, is the interfering Raman background from the high-concentration chemicals used in RIMS that are required by all tissue clearing methods.

It is a common practice in the Raman field to employ commercial Raman-active dyes for multiplexed detection in the fingerprint region (500~1700 cm^{-1})[22]. To study their

spectral compatibility with RIMS, we picked Mitotracker deep red and ATTO740 as two model compounds[16], and used the RIMS from popular tissue clearing methods as ScaleS[23], FOCM[24], Ce3D[25], 3DISCO[26] and uDISCO[27] to represent the final imaging media. As expected, the fluorescence signals of Mitotracker and ATTO740 were background free in all the RIMS used in the test (Extended Fig. 1a). However, the epr-SRS signals of both Mitotracker and ATTO740 suffered from interfering Raman backgrounds in the fingerprint region originated from the RIMS with varying extent (Extended Fig. 1b, c). In particular, the backgrounds from RIMS in 3DISCO and uDISCO completely overwhelmed the signal from Mitotracker. Similarly, ATTO740 signal was largely buried in the background from RIMS in Ce3D. The epr-SRS imaging results can be explained by the relative Raman spectral intensities acquired for RIMS in this fingerprint region (Extended Fig. 1d).

The above incompatibility of commercial Raman-active dyes with tissue clearing urges us to look for spectral features outside the fingerprint region. Epr-SRS imaging also works for specially engineered MARS dyes which uniquely employ π-conjugated triple bonds (hence electronically coupled upon epr-SRS excitation) as the bioorthogonal Raman reporters in the cell-silent spectral region (1800~2800 cm^{-1})[16,19,28]. Due to the structural and spectral similarity of all MARS dyes, we picked a MARS dye as a model system to study the spectral compatibility with those RIMS. Remarkably, the epr-SRS imaging of the MARS dye was free from background interference of all the tested RIMS, indicating MARS dyes were spectrally orthogonal to all the solutions tested (Extended Fig. 1e). This desirable feature emerges because all clearing reagents are Raman-transparent in the spectral range (2000~2400 cm^{-1}) of the reporter triple bonds (Extended Fig. 1f), indicating spectral compatibility of entire MARS palette with all the common RIMS. We hence selected the bioorthogonal MARS dyes over conventional/commercial dyes as the imaging probes for RADIANT.

One-shot 12-color protein imaging with expanded MARS palette

We next expanded the MARS palette for one-shot multiplex immunolabeling. *N*-hydroxy-*succinimidyl-ester* (NHS ester) is a common reactive group to functionalize dyes for subsequent antibody conjugation. Since only four MARS probes were previously synthesized with NHS esters[16] (carbon-cored (C-cored) xanthene structure, blue box in Fig. 2a), we synthesized a new set of NHS-ester-functionalized MARS probes that differ in core atoms, ring numbers and isotope combination on nitrile bonds (Supplementary Fig. 1). After examining the resulting SRS spectra, four more MARS probes of an oxygen-cored (O-cored) scaffold were selected (red box in Fig. 2a) based on optimal spectral separation and peak width (Supplementary Fig. 1 and Supplementary Table 2). Together with the original four C-cored probes, we obtained eight NHS-ester-functionalized MARS probes with distinct epr-SRS peaks (Fig. 2b).

Immunostaining of these MARS probes was then verified under epr-SRS (immuno-eprSRS). Upon conjugating NHS-ester-functionalized MARS probes to secondary antibodies, specific protein targets can be visualized inside cells with diffraction-limited resolution (Fig. 2c, Extended Fig. 2, Supplementary Fig. 2). When applied to tissues, immuno-eprSRS is compatible with multiple protein targets (e.g., NeuN, GFAP, MBP, MAP2, CB) and has

comparable performance to standard immunofluorescence (Fig. 2d, Extended Figs. 3–4, Supplementary Fig.3). Immuno-eprSRS is applicable to common sample preparations including PFA fixed tissues, formalin-fixed paraffin-embedded (FFPE) tissues and frozen tissues (Fig. 2e). Direct immunostaining with MARS conjugated primary antibodies also showed good contrast (Extended Fig. 3c). Besides immunostaining, MARS conjugated lectins allowed us to visualize cell membrane and vasculature by targeting glycoproteins (Extended Fig. 3d). Together, these results indicate that immuno-eprSRS is generally applicable to imaging various protein targets in diverse tissue types under different sample preparations.

We then pursued simultaneous multiplex immuno-eprSRS imaging. As a feasibility test, two MARS probes with the smallest spectral separation (~12 cm^{-1}, one C-cored and one O-cored) can be used together without cross-talk (Extended Fig. 5a), indicating all 8 MARS probes are spectrally separable. Moreover, SRS can be integrated with fluorescence (both confocal and two-photon) as a multi-modality platform (Fig. 2f), benefiting in increased multiplexing power and direct access to well-developed fluorescence probes. We then stained mouse cerebellum thin sections and demonstrated 12-plex protein imaging (Fig. 2g, Extended Fig. 5b–d and Supplementary Note 1). All targets were imaged with expected patterns similar to the single-channel results (Extended Fig. 3). Through established biomarkers, we can identify different cell types such as cerebellar granule neurons (NeuN), purkinje neurons (CB), astrocytes (GFAP) and oligodendrocytes (MBP).

Screening and studying tissue clearing methods for immuno-eprSRS

Next, we sought to develop RADIANT by extending immuno-eprSRS of MARS probes to volumetric imaging. Two-photon excitation of SRS allows for intrinsic 3D optical sectioning and prevents out-of-focus photo-bleaching (Extended Fig. 6). Our main task is thus to identify proper tissue clearing protocols. While volumetric SRS was recently reported for label-free chemical imaging[29], a urea-based clearing protocol was used to preserve lipids, resulting in a compromised clearing ability in thick tissues (Extended Fig. 7a). Besides, urea is known to disrupt antibody-antigen binding affinity[30], thus is less ideal for immunostaining. We hence evaluated several immunolabeling-verified and fast clearing approaches including ScaleS[23], FOCM[24], Ce3D[25], 3DISCO[26] and uDISCO[27]. Signal-to-noise ratios (SNR) of immuno-eprSRS on 40 or 100-μm tissue sections were measured after these clearing procedures, reflecting the joint effect of clearing, staining, probe concentration and stability. We found that DISCO-based methods outperformed others (Fig. 3a), partly due to probe concentration increase mediated by tissue shrinkage. Therefore, we chose DISCO as our basic protocol.

Next, we asked why uDISCO performed better than 3DISCO (Fig. 3a), as tissue shrinkage is similar for both methods. In 3DISCO, the RI matching medium DBE is known to be prone to form peroxides[27] (Fig. 3b and Supplementary Note 2). As shown in the absorption spectra of MARS probes freshly dissolved in the RIMS, a substantial intensity decrease was observed in DBE compared to either BABB or BABB-D4 (BABB:DPE=4:1 in uDISCO) (Fig. 3b, c). Besides, a bluer absorption band appeared in DBE, especially for C-cored probe (Extended Fig. 7b). These results collectively suggested the decomposition of MARS

probes, likely induced by peroxides formed in DBE. Going from solutions to tissue samples, uDISCO also generated better SNR in immuno-eprSRS than 3DISCO (Fig. 3d) and induced less post-clearing fluorescence background (Fig. 3e), in consistent with the solution results.

By virtue of the chemical stability of MARS probes in uDISCO, we achieved 3D immuno-eprSRS imaging on 500-μm thick cerebellum sections with good contrast (Fig. 4a and Extended Fig. 8). In comparison, the contrast of uncleared sample decreases rapidly over a shallow depth of 50–100 μm (Supplementary Fig. 4). Such single-color success can be readily extended to multiplex epr-SRS imaging, thanks to the chemical similarity of all the MARS probes (Fig. 2a). Notably, 8-target volumetric imaging (six SRS and two fluorescence channels) can be carried out in one shot by RADIANT with expected patterns along the entire depth for each channel (Fig. 4b–c and Supplementary Fig. 5, magnified views in Fig. 4c), which already breaks the color barrier for thick tissues (Fig. 1).

Development of rDISCO for MARS dyes

Our insight on MARS probe susceptibility to peroxides provides an opportunity to further improve the clearing method. Starting from uDISCO, we found lowering clearing temperature to 4°C increased SNR (Fig. 5a), as probe decomposition slowed down as temperature decreases[31]. To scavenge peroxides, the uDISCO protocol adds a stable solvent DPE and an antioxidant Vitamin E for better preserving fluorescent proteins[27]. These strategies are also found to work for preserving MARS probes (Fig. 5b). Inspired by these findings, we further screened other common antioxidants in BABB-D4 solution, and found propyl gallate (PG) markedly improved SNR for both O- and C-cored probes (Fig. 5b, c). Indeed, PG is known to be an exceptionally potent antioxidant (~1,000 times more than Vitamin E)[32–34]. Studying the concentration effect of PG (Fig. 5d), we found the SNR of MARS dyes plateaued around 1% PG. Together, we finalized this tailored tissue clearing protocol as BABB-D4 supplemented with 1% PG for clearing under 4°C and named it Raman DISCO (rDISCO).

Finally, we demonstrated RADIANT with rDISCO for improved performance. For immuno-eprSRS on 100-μm sections, rDISCO offered 2.6-fold SNR improvement over uDISCO which was 1.8-fold better than 3DISCO (Fig. 5e), supporting rDISCO as a valuable improvement. Going to 1-mm thick cerebellum sections, we labeled GFAP with C-cored MARS probe and made a comparison between rDISCO and uDISCO (Fig. 5f and Extended Fig. 9a). A fluorescence channel targeting MBP was also included as a reference. Zoomed-in images indicate fine spatial resolution of immuno-eprSRS after rDISCO clearing (Fig. 5g, h). Again, rDISCO offered universal SNR improvements over uDISCO for the entire thickness profile (Fig. 5i) which is 1.8-fold on average for all selected depths (Fig. 5j) and ~2-fold for the center region of the tissue (Extended Fig. 9b).

One-shot multiplexed imaging of millimeter-scale tissues

Encouraged by the SNR improvement with rDISCO, we accomplished one-shot imaging of eleven different targets in a 1-mm-thick cerebellum section from a developing mouse (postnatal day 15, P15) cleared by rDISCO (Fig. 6a and Supplementary Fig. 6). Because all channels were imaged in one round, the resulting images are intrinsically auto-aligned in 3D

without the need of co-registration correction. The one-shot approach has unique advantages for thick tissues in that antibody staining and imaging can be performed for all targets in one shot, thereby circumventing the key limitations (discussed in the Introduction) associated with cyclic immunofluorescence techniques. The results demonstrated here have extended the imaging depth of state-of-the-art cyclic immunofluorescence imaging (achieving 7~12 colors in 100-μm tissues[13–15]) by 10 folds. The improvement is even more (>100 folds) when compared to mass-spectrometry-based methods[5,6].

Versatile analysis of segmentation, spatial correlation, cellular composition, 3D distance and network topology

We next showcased the utility of the multiplexed volumetric images in extracting systems information including regional segmentation, spatial correlation, cellular composition, 3D distance and network topology. First, based on several markers (see Methods for details), we segmented the image into four anatomical layers of the cerebellum—white matter, the granular layer, the Purkinje layer and the molecular layer (Extended Fig. 10a). Next, to acquire an overview of protein-protein correlation, we generated the heatmaps of Pearson's correlation coefficients between different protein pairs with hierarchical clustering for the four layers (Fig. 6b). The correlation we observed is evidently higher than the random level (Extended Fig. 10b). As cerebellar granule cells are the most numerous neurons in the brain with their cell bodies densely packed into the granular layer[35], the neuronal nuclear marker NeuN and the nuclear stain TO-PRO show highly positive correlation in the heatmaps and close clustering in the dendrograms of the granular layer and all layers (Fig. 6b, granular layer and all layers). On the contrary, two cytoskeleton proteins, the astrocyte-specific GFAP and the neuron-specific TUBB3[36] show negative or close-to-zero correlation in the heatmaps and reside far apart in the dendrograms across four anatomical layers (Fig. 6b). These observations capture spatial correlation and clustering with faithful biological meanings.

Cellular composition and 3D distance information can also be obtained. In Fig. 6b, we noticed strong correlation between vimentin (Vim) and GFAP, two major intermediate filaments for astrocytes, particularly in the white matter (r=0.73). To study Vim-GFAP correlation in different anatomical layers, we segmented $Vim^+/GFAP^-$, $Vim^-/GFAP^+$ and $Vim^+/GFAP^+$ cells (Fig. 6c) and performed cell compositional analysis (Fig. 6d, e and Extended Fig. 10c). In the period of rapid myelination (~P0–P21 for mouse), a transition has been reported to occur as vimentin is progressively replaced by GFAP in astrocytes during glial development (Fig. 6c)[37,38]. Hence, $Vim^+/GFAP^-$, $Vim^+/GFAP^+$ and $Vim^-/GFAP^+$ cells will correspond to astrocyte progenitors/radial glia, differentiated astrocytes and mature astrocytes/Bergmann glia[38], respectively (Fig. 6c). Consistently, we found the majority of astrocytes (i.e. $GFAP^+$ cells) co-express vimentin (Fig. 6e, compare the proportion of $Vim^+/GFAP^+$ cells to that of $Vim^-/GFAP^+$ cells), suggesting an early stage of glial development in the P15 mouse, coincident with the time window of myelination[39]. The distance between a cell and its closest blood vessel (cell-to-vessel distance) is a key parameter in the organization and development of the central nervous system, which has to be assessed from volumetric images. We measured the astrocytes-to-vessel distances (for all $GFAP^+$ cells) in our cerebellum sample as 7.8 ± 0.2 μm (Fig. 6f). This distance is in a similar range to that measured in mice somatosensory cortex as 6–10 μm in literature[40]. Notably,

the cell-to-vessel distance is found to exhibit different distributions for three populations of cells, with the mean distances of 8.7 ± 0.2 μm for $Vim^+/GFAP^-$ cells, 5.9 ± 0.2 μm for $Vim^+/GFAP^+$ cells, and 17.0 ± 0.6 μm for $Vim^-/GFAP^+$ cells (Fig. 6f, g); and the relatively close cell-to-vessel distances for $Vim^+/GFAP^-$ and $Vim^+/GFAP^+$ cells suggest that the coordination and interactions between glial progenitors and blood vessels may peak at an early stage of astrocyte differentiation[41,42]. In particular, the closest association of $Vim^+/GFAP^+$ cells with blood vessels (Fig. 6f, g) and their predominant distribution in white matter (Fig. 6d) echo with the essential functions of astrocytes for the integrity of blood brain barrier and white matter vascularization during development[43–45].

Network analysis allows us to explore the underlying architectures and design principles of complex biological systems[46,47]. We analyzed correlation networks of these eleven molecular species for the four anatomical layers (Fig. 6h). First, we calculated two system-level properties of networks—average clustering coefficients and network diameters[46]. The average clustering coefficients range from 0.65 to 0.76 for these five networks. These large, region-independent clustering coefficients indicate modularity of the networks—a group of linked nodes work cooperatively to carry out functions[46]. The network diameters are 2 or 3 for these five networks, exhibiting the “small-world” property[46,47]. Next, we analyzed node importance by calculating the closeness centrality (high centrality implies a central role in the network[48]) and color-coded each node with the centrality score, revealing the network of entire space and specific layers (Fig. 6h). For instance, 5 nodes have high centrality values in the network of all layers: LEL-labeled blood vessels and GFAP-labeled astrocytes maintain the blood-brain barrier and provide nutrients to the nervous tissues[49,50]; ConA and GS-II label specific glycoproteins that are involved in cell differentiation and development[51]; GABBR2 is a key inhibitory receptor for synaptic transmission[52]. Noteworthily, the node TUBB3 exhibit a high centrality score only in the Purkinje layer, in contrast to its low centrality scores in the other three layers. This distinct topology of TUBB3 suggests its special role for Purkinje cells. Indeed, TUBB3 was the only β-tubulin isotype expressed in Purkinje cells, with an essential role in axon guidance and maintenance[53,54]. Taken together, mapping 3D spatially-resolved correlation networks of proteins has gained insight into the organizational principles of complex tissues. Such analysis may be extended to identify potential molecular targets for diagnostic and therapeutic applications.

Discussion

High-content, large-context protein imaging is becoming increasingly critical in life science. Towards this goal, extensive efforts have been devoted to developing multiplexed protein imaging in large three-dimensional biological systems. However, current protein imaging methods are constrained by a general trade-off between the achievable content (i.e., high multiplexing) and context (i.e., thick samples). As we summarize in Fig. 1, all the existing multiplexed protein imaging techniques are confined to shallow depths (<100 μm, i.e., poor context), whereas protein imaging in thick tissues (> 100 μm) cannot exceed ~5 colors (i.e., poor content), limited by the fluorescent “color barrier”. Due to this content-context trade-off, highly multiplexed volumetric protein imaging remains challenging.

Different from these precedents, our approach is a one-shot optical method without the compromise between depth and multiplexity (Supplementary Table 4), by leveraging innovations in coherent Raman microscopy, probe chemistry and tissue engineering. Specifically, we exploited the coupling between tissue clearing technology and epr-SRS microscopy, the most sensitive vibrational imaging modality to date. After observing the interfering background from the tissue clearing reagents with conventional Raman dyes, we reported new bioorthogonal vibrational probes for immuno-eprSRS, offering good detectability (comparable to standard immunofluorescence), fine spatial resolution, general sample compatibility and scalable multiplexity. In addition, after screening and studying common tissue clearing methods for volumetric immuno-eprSRS, we developed a MARS-probe tailored tissue clearing method rDISCO. Combining these developments together, we have achieved one-shot multiplex (>10) protein imaging within a single tissue of millimeter thickness for the first time, to our best knowledge. Systematic analyses of the images showcased their utility in extracting regional segmentation, spatial correlation, cellular composition, 3D distance and network topology. Conclusively, our RADIANT approach of coupling one-shot epr-SRS microscopy of MARS probes with tailored tissue clearing circumvents practical complexity in cyclic methods and largely improves the throughput, thereby opening up a new territory for high-content, large-context protein imaging (Fig. 1).

Future optimizations of RADIANT reside along several fronts. First, penetration depth and staining uniformity of current passive antibody permeation are suboptimal and dependent on the specimen size and abundance of target proteins, preventing our demonstration going beyond 1-mm thickness. Recent innovations on rapid and uniform immunolabeling using facilitated transport[13,55] are promising to extend the depth and greatly shorten the entire pipeline. Second, a relatively long pixel dwell time (60 μs) makes the net acquisition time of Fig.6a about 4 hrs. Explorations on *in situ* signal amplification techniques[56,57] are expected to significantly boost the imaging speed and throughput. Third, current multiplexity of 11 channels are jointly limited by the availability of source species of secondary antibodies and resolvable Raman probes. Further increased plex (>20) can be foreseen through introducing functionalized polyyne-based Raman probes[58], as well as systematic validation of a library of Raman-probe-conjugated primary antibodies. Fourth, pursing RNA and DNA as the targeted molecules will presumably make RADIANT a spatial-resolved pan-omics tool.

Our high-content, large-context protein imaging approach provides intrinsic advantages for molecular profiling in intact tissues as nondestructive, cycle-free and registration-free. Notably, a fully integrated multimodal SRS/fluorescence research microscope similar to the system in this work has already been commercialized (Supplementary Note 1), providing direct instrumental accessibility to biomedical researchers. Overall, we envision RADIANT will be valuable for deciphering complex biological systems, such as building tissue atlases, phenotyping tumor microenvironment and profiling brain circuits.

Methods

Protein-MARS probe conjugation

NHS-ester-functionalized MARS probes were stored at a concentration of 10 mM in DMSO under −20 °C, protecting from light and moisture. To perform protein-dye conjugation,

dye solutions were first diluted in DMSO to a concentration of 2 mg/mL. Conjugation buffer was prepared as 0.1 M $NaHCO_3$ in PBS buffer with pH adjusted to 8.3. Highly cross-absorbed secondary antibodies were buffer exchanged and concentrated to 2 mg/mL in the conjugation buffer. A 50 μL dye-NHS solution was slowly added to a 0.5 mL secondary antibody solution under stirring. For primary antibody labeling, the protein concentration was adjusted to 1 mg/ml and the molar ratio of dye/protein was usually 10–15. Lectins were first dissolved in conjugation buffer as 2 mg/ml. For Wheat Germ Agglutinin (WGA) labeling, a 10 μL 2 mg/ml dye-NHS solution was added to a 0.5 mL 2 mg/ml WGA solution. For *Lycopersicon Esculentum* Lectin (LEL) labeling, a 25 μL 2 mg/ml dye-NHS solution was added to a 0.5 mL 2 mg/ml LEL solution. Reactions were all incubated at room temperature for 1 h under constant mild stirring. Labeled proteins were further separated from unreacted dyes by gel permeation chromatography using Sephadex™ G-25 (G25150 SIGMA) resins with a column of 1-cm diameter and over 12-cm length. Purified protein solution was centrifuged to remove potential precipitates and further concentrated with Amicon® Ultra Centrifugal Filters (UFC501096, EMD, Millipore). A final concentration of ~2 mg/mL protein solution (for secondary antibodies and lectins) were prepared in stocking buffer (30% glycerol and 5 mM sodium azide in PBS) and stored at −20 °C. The degree of labeling (DOL, i.e. dye-to-protein ratio) were measured with UV-Vis spectrum using Tecan Infinite 200 Reader with a NanoQuant Plate. DOL on secondary antibodies is about 3.

Cell culture

Human HeLa (ATCC CCL-2), COS-7 (ATCC CRL-1651) cells were cultured in DMEM (Invitrogen 11965) supplemented with 10% FBS (Invitrogen 10082) and 1× penicillin/streptomycin (Invitrogen 15140). Human MCF7 (ATCC HTB-22) cells were cultured in EMEM (ATCC 30–2003) supplemented with 10% FBS and 1× penicillin/streptomycin.

Mouse sample preparation

Brain tissues.—Animal experimental protocol (AC-AABD1552) was approved by the Institutional Animal Care and Use Committee (IACUC) at Columbia University. Wild type male and female mice (C57BL/6, 15–25 days old, Jackson Lab) were fully anesthetized using isoflurane, then sacrificed with cervical displacement and immediately perfused with 4% paraformaldehyde (PFA) in PBS transcranially. The brain was extracted and fixed in 4% PFA in PBS at 4 °C for 24 h. After that, the brain was immersed in PBS at 4 °C for 24 h to remove PFA. The cerebellum was embedded in 7% agarose gel and sectioned into 40 μm, 100 μm, 500 μm, and 1 mm thick coronal slices using a vibratome (VT1000S, Leica). Agarose was removed by a tweezer before staining.

Pancreas tissues.—Animal procedures were performed under protocols approved by the IACUC of Colorado Anschutz Medical campus (#00024). Wild type male and female mice (C57BL/6, 8–12 weeks old, Jackson Lab) were anesthetized by I.P. injection of Ketamine (80 mg/kg) and Xylazine (16 mg/kg) until no longer reactive to toe pinch. Pancreata were dissected and mice were then euthanized by exsanguination and/or Bilateral thoracotomy. Pancreata were fixed in PFA (4% in PBS) at 4 °C rocking for 16–20 h, washed in 4 °C PBS to remove PFA, and embedded in OCT blocks. 8 μm sections were then taken for staining.

Stimulated Raman scattering (SRS) and fluorescence integrated imaging platform

SRS and fluorescence imaging were performed on an inverted laser scanning microscope (Olympus FV1200) using a 25× water-immersion objective lens (Olympus XLPlan N, 1.05 NA, MP, WD = 2 mm).

For SRS imaging, two synchronized 6-ps lasers (called pump and Stokes beams) with 80-MHz repetition rate are provided by a picoEmerald system from APE (Applied Physics & Electronic, Inc.). Pump beam is tunable from 720–990 nm through both temperature control of the nonlinear crystal and a Lyot filter. Stokes beam is fixed at 1064.2 nm. The intensity of the Stokes beam was modulated sinusoidally by a built-in electro-optic modulator (EOM) at 8 MHz with a modulation depth of more than 90%. Spatially and temporally-overlapped pump and Stokes beams were coupled into the laser-scanning microscope. After passing through the specimens, forward-going pump and Stokes beams were collected with an IR-coated oil condenser (1.4 NA, Olympus). Stokes beam were completely filtered with two high-optical-density bandpass filter (890/220 CARS, Chroma Technology) and transmitted pump beam was detected by a large-area (10 mm×10 mm) Si photodiode (FDS1010, Thorlabs). The output current of the photodiode was then sent to a fast lock-in amplifier (HF2LI, Zurich Instruments) for signal demodulation. For immuno-eprSRS imaging, the laser power was set as P_{pump}=17 mW, P_{Stokes}=50 mW for C-cored MARS probes and P_{pump}=17 mW, P_{Stokes}=67 mW for O-cored MARS probes. SRS images were generated through Kalman filtering of 10–30 serial frames with the pixel dwell time of 4 μs. The time constants of lock-in amplifier were chosen as 2–4 μs. Pixel sizes were chosen as about 0.25–1 μm. For volumetric imaging, the step size in z was 5 μm.

For two-photon fluorescence, DAPI dye or Alexa Fluor 350 were excited by the SRS pump laser at 760 nm. The backward fluorescence was detected after passing through a 690-nm short-pass filter, reflected by a 570-nm long-pass dichroic with a collection band of 410–490 nm. For confocal fluorescence, green channel is excited by argon laser (488 nm) with a collection band of 505–520 nm; red channel is excited by HeNe(G) laser (543 nm) with a collection band of 560–620 nm; far-red channel is excited by LD laser (635 nm) with a collection band of 655–755 nm. Multichannel photomultiplier tube (PMT) was used for fluorescence detection. Pixel sizes were chosen as about 0.25–1 μm and pixel dwell time were set as 2–4 μs.

Immuno-eprSRS staining on thin tissue sections

For PFA fixed mouse cerebellum thin sections, 40-μm thick sections from P15-P40 young mice were used. The staining was performed on the floating tissues in a 4-well plate. Samples were permeabilized and blocked with blocking buffer (5% donkey serum, 0.5% Triton X-100 in PBS) at room temperature for 30 min. After blocking, samples were incubated with primary antibody (typical dilution, 1:100) in staining buffer (2% donkey serum, 0.5% Triton X-100 in PBS) at 4 °C for 1–2 d, followed by washing at room temperature for 5–10 min in PBS with 0.5% Triton X-100 (0.5% PBST) three times. Samples were then blocked in blocking buffer for 30 min, followed by incubating with MARS-conjugated secondary antibody (typical dilution, 1:100) in staining buffer at 4 °C for

1–2 d. After staining, the samples were washed at room temperature for 5–10 min in 0.5% PBST three times.

Frozen mouse pancreatic tissue slides were stored at −80 °C. Specimens were first equilibrated to room temperature and held in PBS buffer before staining. The staining processes were performed on slides with a similar protocol as described above for PFA tissues, with the following changes. A Triton X-100 concentration of 0.3% was used for blocking buffer, staining buffer and sample washing. Incubation time for both primary and secondary antibodies is 18 h.

FFPE human kidney slice used in this study was purchased from Biomax (HuFPT072). FFPE tissue slides were first baked at 60 °C for 10 min. Samples were sequentially placed in following solutions (in a 50 mL Falcon tube) for deparaffinization and rehydration with 3 min each time at room temperature under mild shaking: (1) xylene two times, (2) ethanol two times, (3) 95 vol% ethanol in DI water two times, (4) 70 vol% ethanol in DI water two times, (5) 50 vol% ethanol in DI water one time, (6) DI water one time. For antigen retrieval, the specimen was first transferred into a glass jar filled with 20 mM sodium citrate (pH=8.0) at 100 °C, followed by a quick transfer of the jar to a 60 °C incubation chamber for 45 min. After that, the specimen was washed at room temperature with DI water for 5 min. The staining processes followed the same protocol as the frozen tissues.

For imaging specimen preparation, PFA fixed tissue sections were transferred to Superfrost glass slide and all specimens were mounted in ProLong Gold antifade (ThermoFisher, P10144) with a glass coverslip, secured with nail polish.

Twelve-target mouse cerebellum imaging

Staining.—See Fig. 2g and Extended Data Fig. 5c–d. The staining processes followed the sample protocol as PFA fixed thin tissue sections above with three rounds of antibody incubation. First round: anti-NeuN antibody (rabbit, dilution 1:50), anti-β-III tubulin antibody (chicken, dilution 1:50), anti-Calbindin antibody (mouse, dilution 1:40), anti-GABBR2 antibody (guinea pig, dilution 1:40), anti-MBP antibody (rat, dilution 1:20), anti-GFAP antibody (goat, dilution 1:50) and MARS2242-conjugated WGA (1:50). Second round: MARS2228-conjugated donkey anti-rabbit IgG antibody, MARS2220-conjugated donkey anti-chicken IgY antibody, MARS2145-conjugated donkey anti-mouse IgG antibody, MARS2212-conjugated donkey anti-guinea pig IgG antibody, MARS2188-conjugated donkey anti-rat IgG antibody and MARS2159-conjugated donkey anti-goat IgG antibody with a dilution of 1:50. Third round: Alexa Fluor 596-conjugated anti-TH antibody (mouse, dilution 1:50), Alexa Fluor 488-conjugated anti-VGluT1 antibody (mouse, dilution 1:50) and MARS2176-conjugated anti-α tubulin antibody (mouse, 0.5 mg/mL, dilution 1:40). Between the second and the third round of antibody incubation, samples were further blocked in 5% normal mouse serum, 0.5% Triton X-100 in PBS at RT for 1 h. The specimens were futher stained with NucBlue and Phalloidin-Alexa Fluor 647 and embedded in the ProLong Gold antifade medium for imaging.

Spectral unmixing.—A linear-combination algorithm was applied on multiplexed epr-SRS data set to remove potential cross-talks between different channels[16]. For *N*-channel

epr-SRS measurement with N MARS probes (N=8 here), measured signals ($\boldsymbol{S}$) can be expressed as $\boldsymbol{S}=M\boldsymbol{C}$, where $\boldsymbol{C}$ is the MARS probe concentrations and M is a $N\times N$ matrix determined by Raman cross-sections of MARS probes. Matrix M was measured experimentally on single-color immuno-eprSRS labeled with different MARS probes. MARS probe concentrations were therefore determined using $\boldsymbol{C} = M^{-1}\boldsymbol{S}$.

Clearing method screening for immuno-eprSRS on MARS probes

Staining.—Samples were first washed with 0.2% PBST at room temperature on a shaking platform for 1h twice, followed by incubation in 20% DMSO, 0.2% Triton X-100 in PBS at 37 °C on a shaking platform overnight. The tissues were incubated in 0.1% Tween-20, 0.1% Triton X-100, 0.1% deoxycholate, 0.1% NP40, and 20% DMSO in PBS at 37 °C on a shaking platform overnight. The tissues were washed with 0.2% PBST at room temperature on a shaking platform for 1 h twice. The tissues were permeabilized with 0.5% PBST at 37 °C on a shaking platform overnight, and then permeabilized and blocked with blocking buffer (5% donkey serum, 0.5% Triton X-100 in PBS) at 37 °C on a shaking platform for 3 d. The tissues were incubated with anti-MBP antibody (rat, dilution 1:20) or anti-GFAP antibody (goat, dilution 1:40) diluted in staining buffer (2% donkey serum, 0.5% Triton X-100 in PBS) at 37 °C on a shaking platform for 2 d, and then washed with 0.5% PBST at 37 °C on a shaking platform for 1 d (the solution was changed several times in between). Then the tissues were incubated with MARS2200-conjugated donkey anti-rat IgG antibody (dilution 1:50), MARS2228-conjugated donkey anti-goat IgG antibody (dilution 1:40), or MARS2159-conjugate donkey anti-goat IgG antibody (dilution 1:40) diluted in staining buffer at 37 °C on a shaking platform for 2 d. The tissues were washed with 0.5% PBST at 37 °C on a shaking platform for 3 h. The tissues were then incubated in PBS at 4 °C overnight. After that, the tissues were cleared with published tissue clearing methods, including ScaleS[23], FOCM[24], Ce3D[25], 3DISCO[26] and uDISCO[27] as previously described, or with different tissue clearing conditions explored in this work. The cleared tissues were mounted on glass slides in a pool created by dental cement and filled with the corresponding refractive index matching solutions and covered with a glass coverslip for SRS imaging.

Quantification.—The signal-to-noise ratios of the raw images were quantified as the main criterion to evaluate different tissue clearing methods. Specifically, the signal-to-noise ratio was calculated as (intensity of the labelled structure/cell – intensity of the background) / standard deviation of the background. The background was measured from the same tissue where no stained pattern appears under the same imaging condition. Thus, the noise is composed of both instrumental noise and sample noise. The signal-to-noise ratios of multiple regions of interest were quantified and presented as mean±s.d. Regions of interest were manually selected with correct localization pattern and from a similar depth.

rDISCO (Raman DISCO) clearing procedure

The immune-labelled tissues were first dehydrated in *tert*-butanol/DI water series as 30 vol%, 50 vol%, 70 vol%, 80 vol%, 90 vol% *tert*-butanol; 2 h each at room temperature on a rotator. Then the tissues were incubated in 96 vol% *tert*-butanol in water at room temperature on a rotator overnight. The tissues were incubated in pure *tert*-butanol at room temperature on a rotator for 2 h. The tissues were incubated in the refractive index matching

solution, which was prepared by mixing BABB (benzyl alcohol and benzyl benzoate was mixed at a ratio of 1:2 and purified by column chromatography using aluminum oxide) with diphenyl ether at a ratio of 4:1 and adding 1% propyl gallate (w/v), at 4 °C for 2 h. The tissues were mounted in the same refractive index matching solution for SRS imaging.

Pre-processing and staining of thick tissue sections

Sample pre-processing.—The pre-processing protocol was adapted from the sample pretreatment procedures in iDISCO[12]. For initial processing, tissue samples were washed with 0.2% PBST at room temperature on a shaking platform for 1 h twice, and then incubated in 20% DMSO in 0.2% PBST at 37 °C on a shaking platform overnight. The tissues were incubated in 0.1% Tween-20, 0.1% Triton X-100, 0.1% deoxycholate, 0.1% NP40, and 20% DMSO in PBS at 37 °C on a shaking platform overnight. The tissues were washed with 0.2% PBST at room temperature on a shaking platform for 1 h twice. The tissues were further permeabilized with 0.5% PBST at 37 °C on a shaking platform overnight and followed by blocking/permeabilization with 5% donkey serum in 0.5% PBST at 37 °C on a shaking platform for 6 d (the solution was changed once after 3 d). After this, the tissue slices were ready for immunostaining.

Thick sample staining.—The staining processes followed similar procedures as thin tissue with varied time and probe concentrations. Detail descriptions can be found in Supplementary Methods.

Three-dimensional reconstruction

Raw volumetric data were unmixed into specific channels using the linear combination algorithm as mentioned above. A median filter was applied to the unmixed images for noise reduction. A Fiji plugin[59] was then applied to the images for attenuation correction. The open radius was set to 0.5. After correction, the images were volume-rendered in the mode of maximal intensity projection using Imaris (Bitplane).

Three-dimensional segmentation and quantitative analyses

Raw volumetric data went through linear unmixing, noise reduction with a median filter, and attenuation correction as mentioned above. Based on the channels of MBP, NeuN, and GABBR2, the image was segmented manually using the “Contour” tool in Imaris into four anatomical layers—white matter, the granular layer, the Purkinje layer, and the molecular layer. The segmentation results were exported from Imaris as four binary masks. After the image was median-filtered using a radius of 2 pixels and thresholded with Otsu’s method, Pearson correlation coefficients were calculated between specific protein channels in the four layers and presented as heatmaps using custom-written MATLAB (MathWorks) scripts. As the MBP channel had no signals in the Purkinje layer and the molecular layer after thresholding, correlation analysis was performed with the rest 10 channels without the MBP channel for these two layers (Fig. 6b). Vimentin positive and GFAP positive cells were segmented using Imaris. The GFAP positive cells that did not touch vimentin positive cells were defined as $Vim^{-}/GFAP^{+}$ cells. The vimentin positive cells that did not touch GFAP positive cells were defined as $Vim^{+}/GFAP^{-}$ cells. The GFAP positive cells that touched vimentin positive cells and the vimentin positive cells that touched GFAP

positive cells were merged into one channel and segmented as $Vim^+/GFAP^+$ cells. The proportions of $Vim^-/GFAP^+$, $Vim^+/GFAP^-$, and $Vim^+/GFAP^+$ cells in the four layers were quantified using the shortest distances to the segmented four layers (A negative shortest distance meant the cell was inside the layer. Cells that spanned multiple layers were excluded from this analysis). Blood vessels were segmented from the LEL channel using Imaris. Shortest distances from $Vim^-/GFAP^+$, $Vim^+/GFAP^-$, and $Vim^+/GFAP^+$ cells to the blood vessels were quantified using Imaris. Correlation-based network graphs were plotted in the four layers using custom-written MATLAB (MathWorks) scripts. Specifically, the "graph" function in MATLAB was used with Pearson correlation coefficients as the input. Self-loops and negative correlation coefficients were discarded. Closeness node centrality was calculated with the "centrality" function and color-coded in each node. The node size was set to be directly proportional to the degree of each node. Network diameters were calculated with the "distances" function. Average clustering coefficients were calculated with the "clusteringcoef" function in the Graph package[60].

Statistics and Reproducibility

Statistical analysis was carried out using GraphPad Prism 7 and OriginPro 8. Data are presented as mean±s.d. or mean±s.e.m. with statistical significance if required (not significant $P \geq 0.05$, $^*P < 0.05$, $^{**}P < 0.01$, $^{***}P < 0.001$, $^{****}P < 0.0001$). In Fig. 5i, $P = 3.0\times10^{-5}$, 9.3×10^{-5}, 1.4×10^{-3}, 8.4×10^{-4}, 4.6×10^{-4}, 2.7×10^{-4}, 1.3×10^{-4}, 7.7×10^{-5}, 3.8×10^{-5}, 1.1×10^{-4}, 3.5×10^{-4}, 4.9×10^{-7}, 1.8×10^{-3}, 2.1×10^{-4}, 1.2×10^{-3}, 2.8×10^{-3}, 3.8×10^{-4} and 7.6×10^{-4}. In Fig. 6f, $P = 8.2\times10^{-87}$ for $Vim^-/GFAP^+$ and $Vim^+/GFAP^+$, 2.2×10^{-55} for $Vim^-/GFAP^+$ and $Vim^+/GFAP^-$, 1.6×10^{-24} for $Vim^+/GFAP^+$ and $Vim^+/GFAP^-$. Other exact *P* values are in the figure legends. In Fig. 5b, e, 6f, *P* values were calculated from multiple comparisons test with one-way ANOVA followed by Holm-Bonferroni's *post hoc* test on comparing the mean of each column with the mean of every other column. In box plot (Fig. 5j), center indicates the median; the bottom and top edges of the box indicate the 25^{th} and 75^{th} percentiles, respectively; the whiskers extend to the minimum and maximum data points. All values of *n* are provided in the figure legends. Statistical source data for Fig. 3, 5, 6 are provided in Source Data. Experiments in Fig. 2c, d, e, g and Extended Data Fig. 1–5 were repeated 3–5 times independently with similar results. Experiments in Fig. 4a, c, 5f and Extended Data Fig. 8 were repeated three times technically on two tissue blocks with similar results.

Extended Data

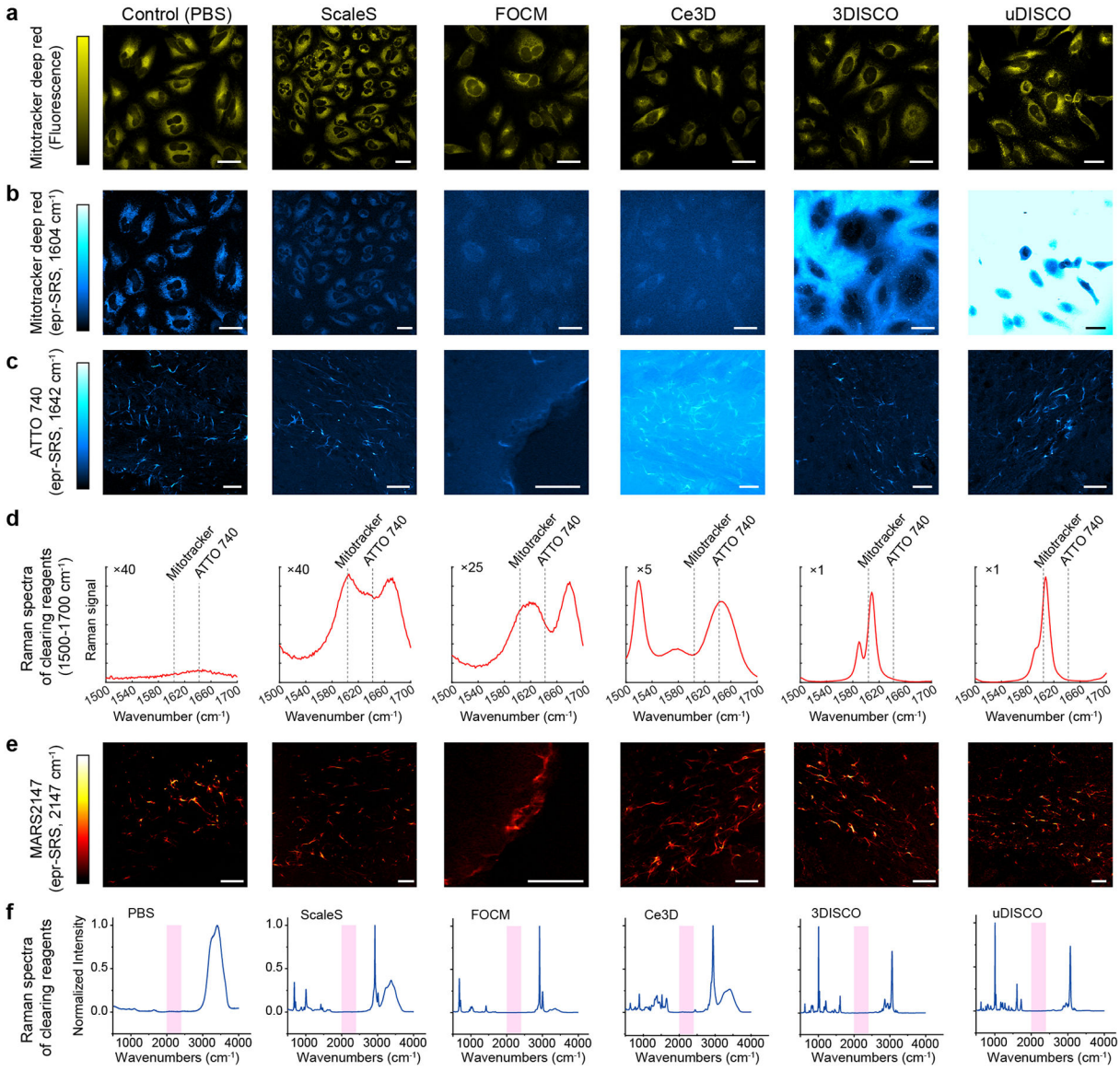

Extended Data Fig. 1. Testing spectral compatibility between Raman-active dyes and tissue clearing methods

a, **b**, Fluorescence (**a**) and epr-SRS imaging at 1604 cm^{-1} (**b**) of Mitotracker deep red FM (Invitrogen M22426)-stained fixed HeLa cells imaged in different RIMS. **c**, epr-SRS imaging at 1642 cm^{-1} of ATTO 740 stained GFAP on PFA-fixed mouse brain tissue inside different RIMS. **d**, Raman spectra of PBS and RIMS only at 1500–1700 cm^{-1} (spectral window for vibrational peaks of most commercial dyes). Some spectra were amplified by certain folds (number inside) to plot them under a same scale. **e**, epr-SRS imaging at 2147 cm^{-1} of MARS2147 stained GFAP on PFA-fixed mouse brain tissue inside different RIMS. **f**, Full Raman spectra of tissue clearing reagents. The pink area indicates the interested spectral window (2000–2400 cm^{-1}), in which the nitrile-bond reporters in MARS probes

vibrate. Spectra in (**d**) and (**f**) were measured with spontaneous Raman spectroscopy. Scale bars, 40 μm.

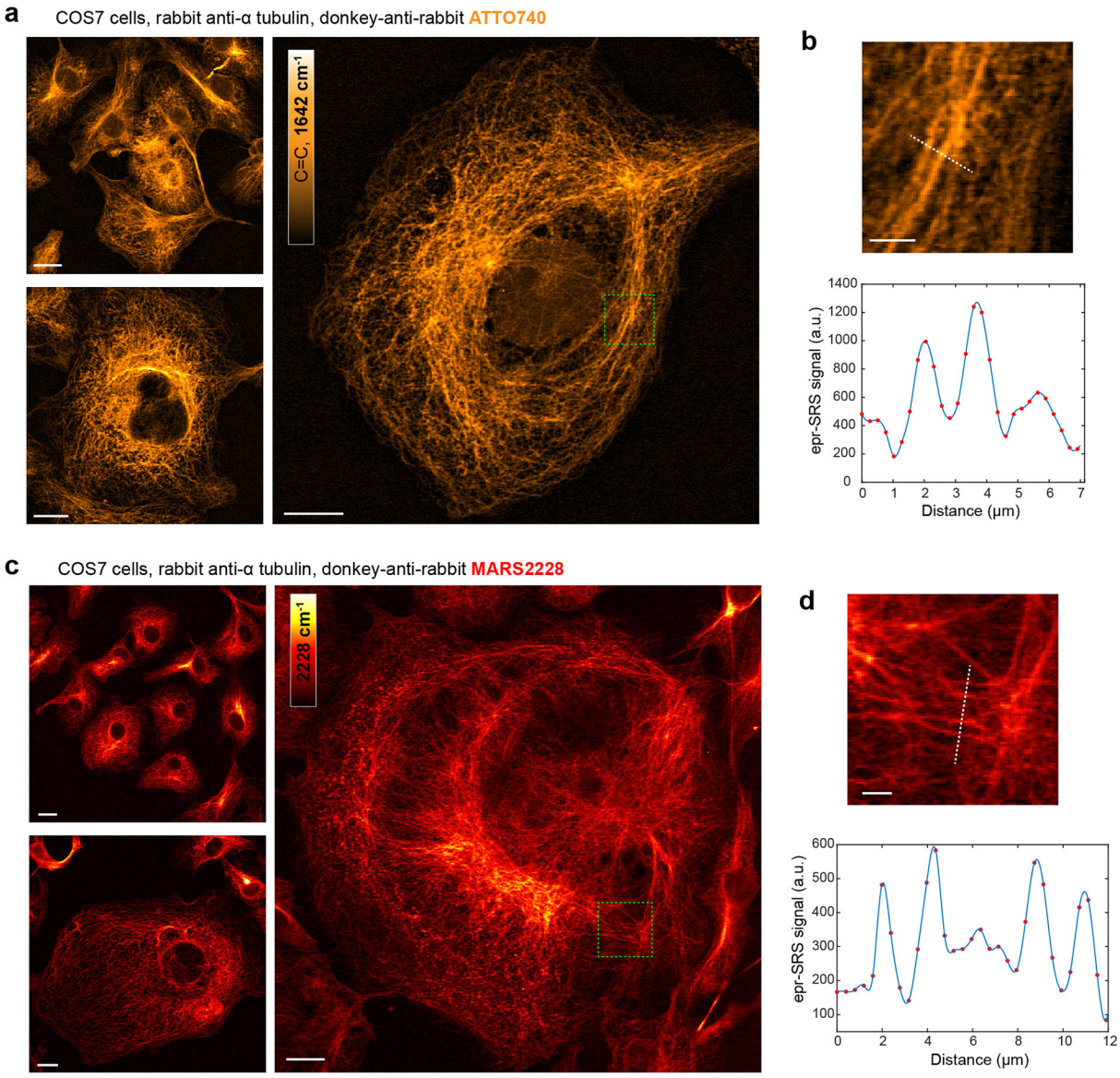

Extended Data Fig. 2. Demonstration of fine resolution of immuno-eprSRS imaging

α-tubulin in COS7 cells were stained with commercial dye ATTO 740 (**a–b**) and MARS2228 (**c–d**). **(b**, **d)** Magnified regions outlined by the green box in (**a**, **c**), respectively. Below, epr-SRS signal along the white dotted line cut in the magnified images; curves were drawn with a spline fit. Scale bars, 20 μm in (**a**, **c**); 5 μm in (**b**, **d**).

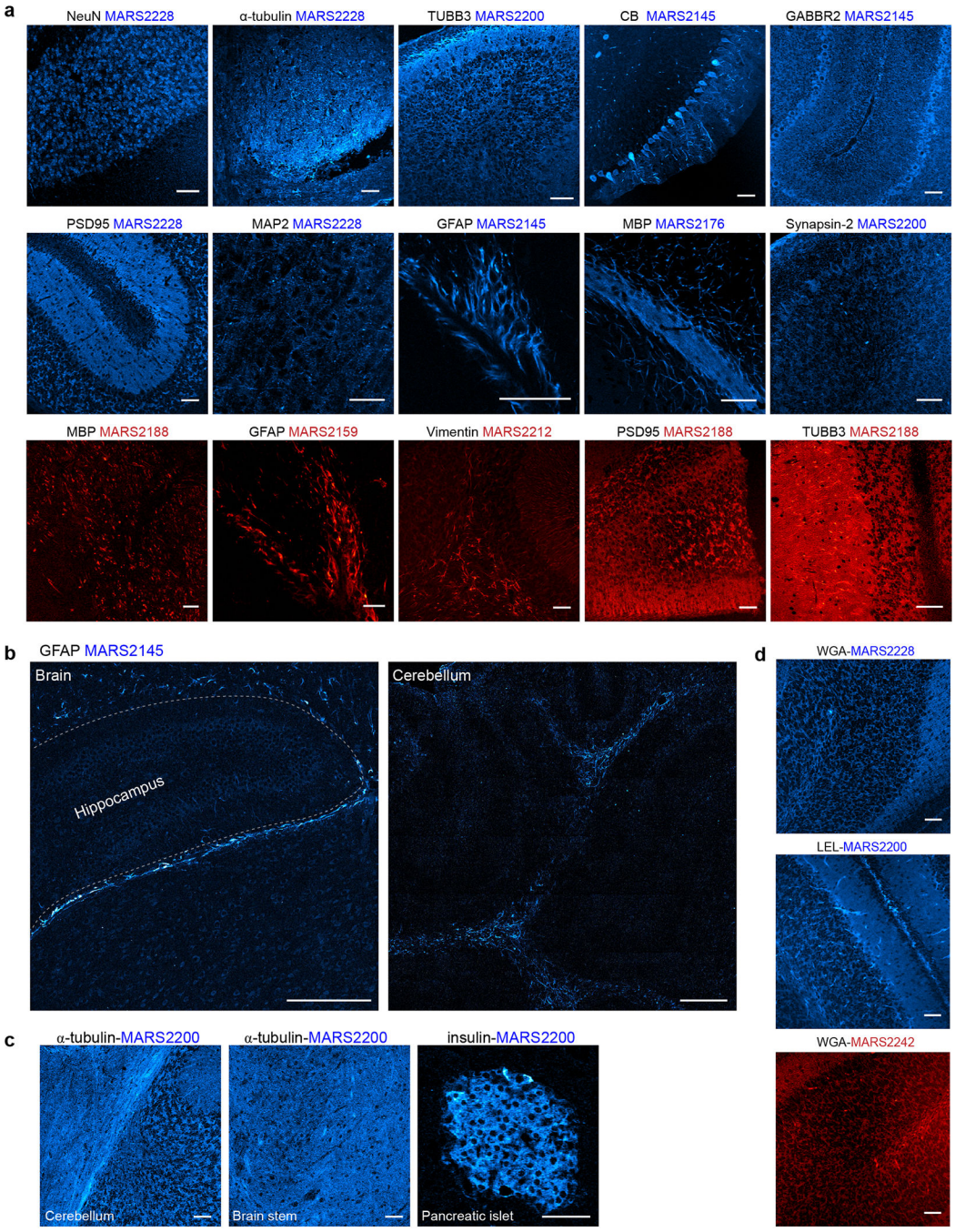

Extended Data Fig. 3. Immuno-eprSRS imaging with MARS probes in tissue samples

a, Multiple protein targets are compatible with immuno-eprSRS with C-cored MARS probes (in blue) and O-cored MARS probes (in red). Targeted proteins were stained on PFA-fixed mouse brain or cerebellum sections (40-μm thick) with indirect immunostaining. **b**, Mosaic imaging with motorized sample stage. NeuN, neuronal nuclei; TUBB3, β-III-tubulin; CB, calbindin; GABBR2, GABA B receptor 2; PSD95, postsynaptic density protein 95; MAP2, microtubule associated protein 2; GFAP, glial fibrillary acidic protein; MBP, myelin basic protein. **c**, Direct immunostaining with MARS-probe conjugated primary antibodies. **d**,

MARS probe-conjugated lectin staining on PFA-fixed cerebellum tissue sections. WGA, wheat germ agglutinin; LEL, *Lycopersicon Esculentum* lectin. More antibody information is in Supplementary Table 3. Scale bars, 50 μm in (**a**) and (**c–d**); 200 μm in (**b**).

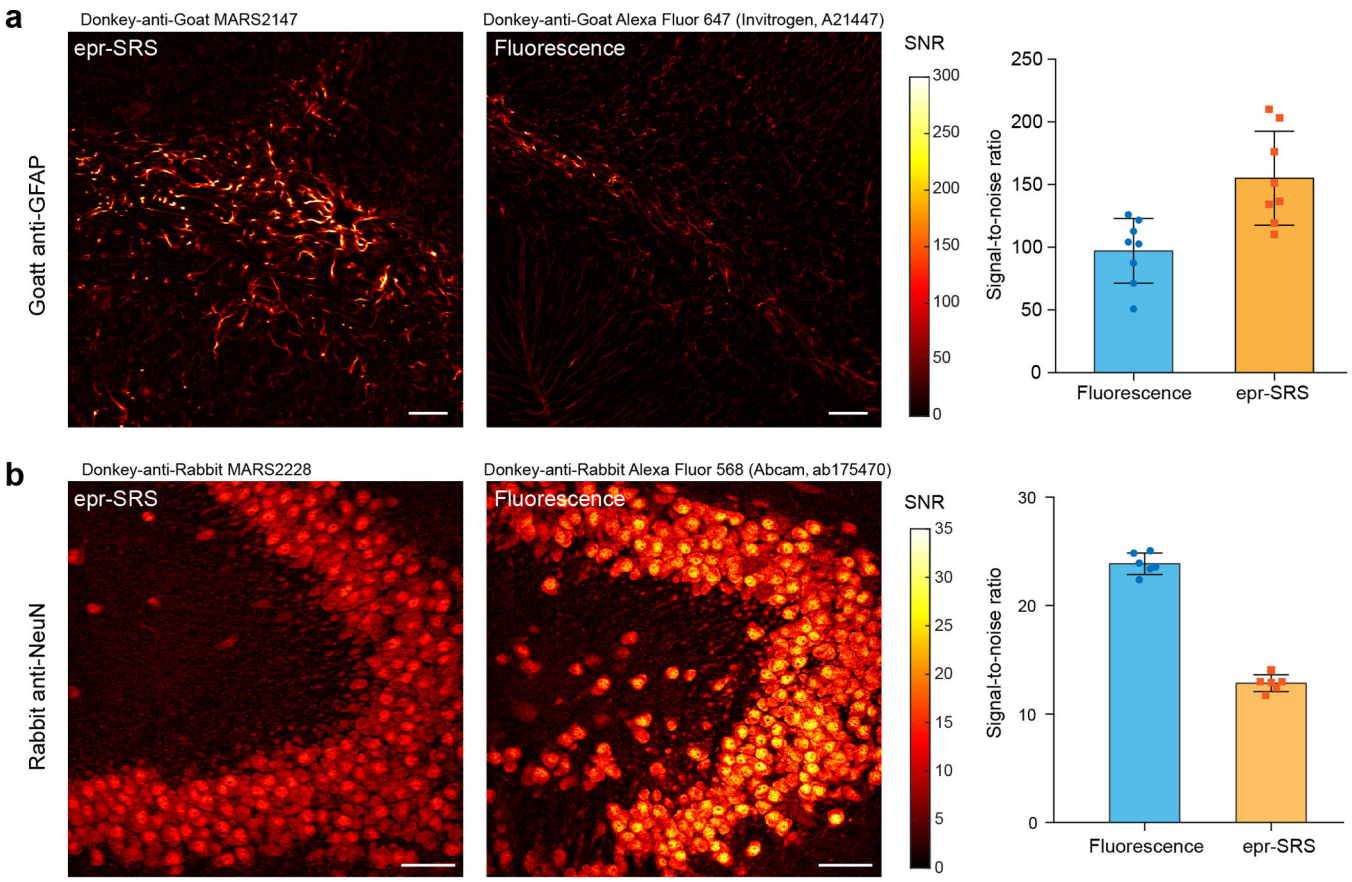

Extended Data Fig. 4. Quantitative comparison of the signal-to-noise ratios of immuno-eprSRS with standard immunofluorescence

a, Immunostained GFAP in 40-μm thick mouse brain tissue. **b**, Immunostained NeuN in 40-μm thick mouse brain tissue. Each data point of the signal was calculated as the averaged fluorescence/epr-SRS signal of individual nucleus for NeuN or individual astrocytes for GFAP; the noise was measured as the s.d. from tissue areas without stained structures. Pixel dwell time is 2 μs for fluorescence and 80 μs for epr-SRS. Scale bars, 50 μm.

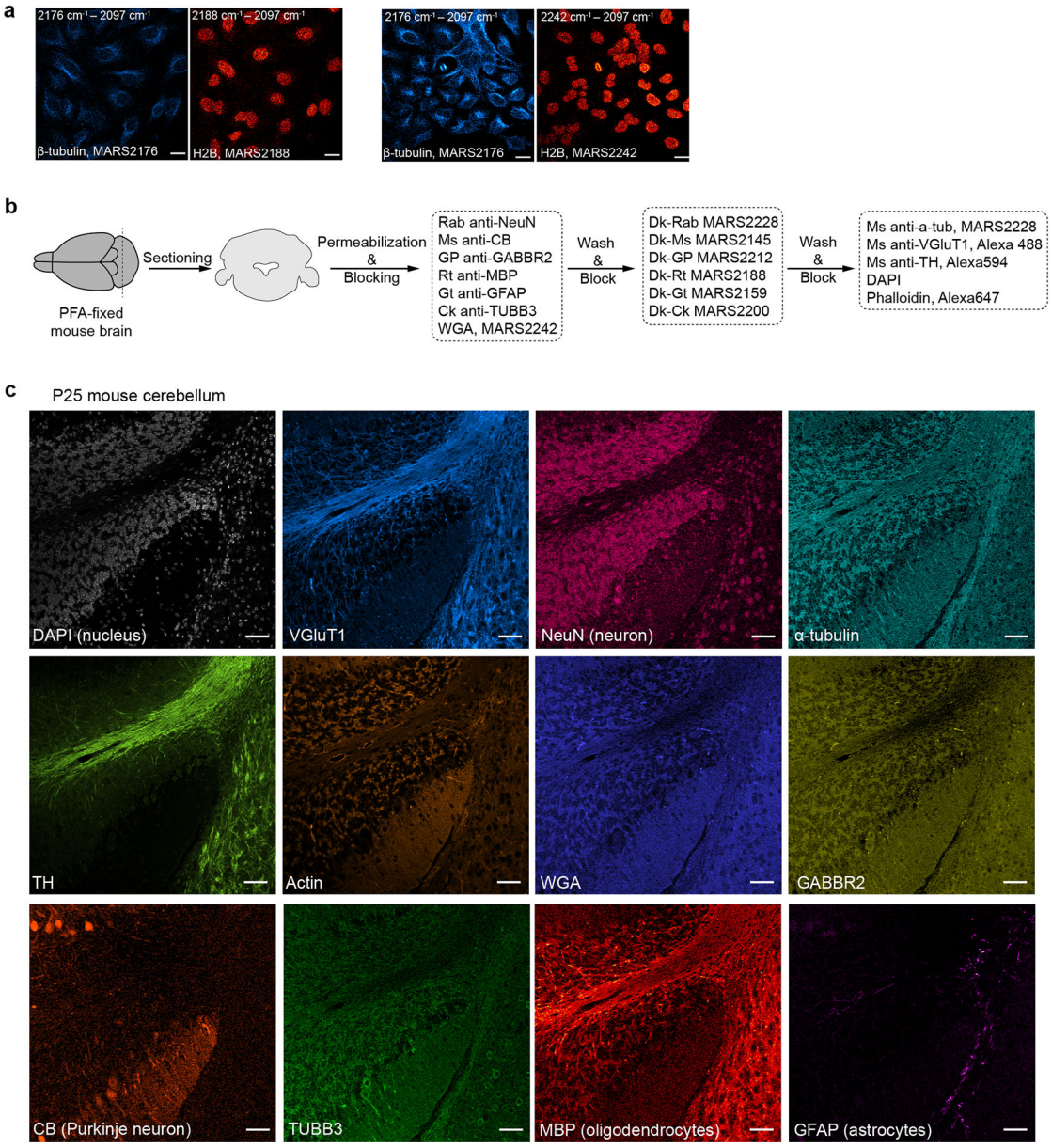

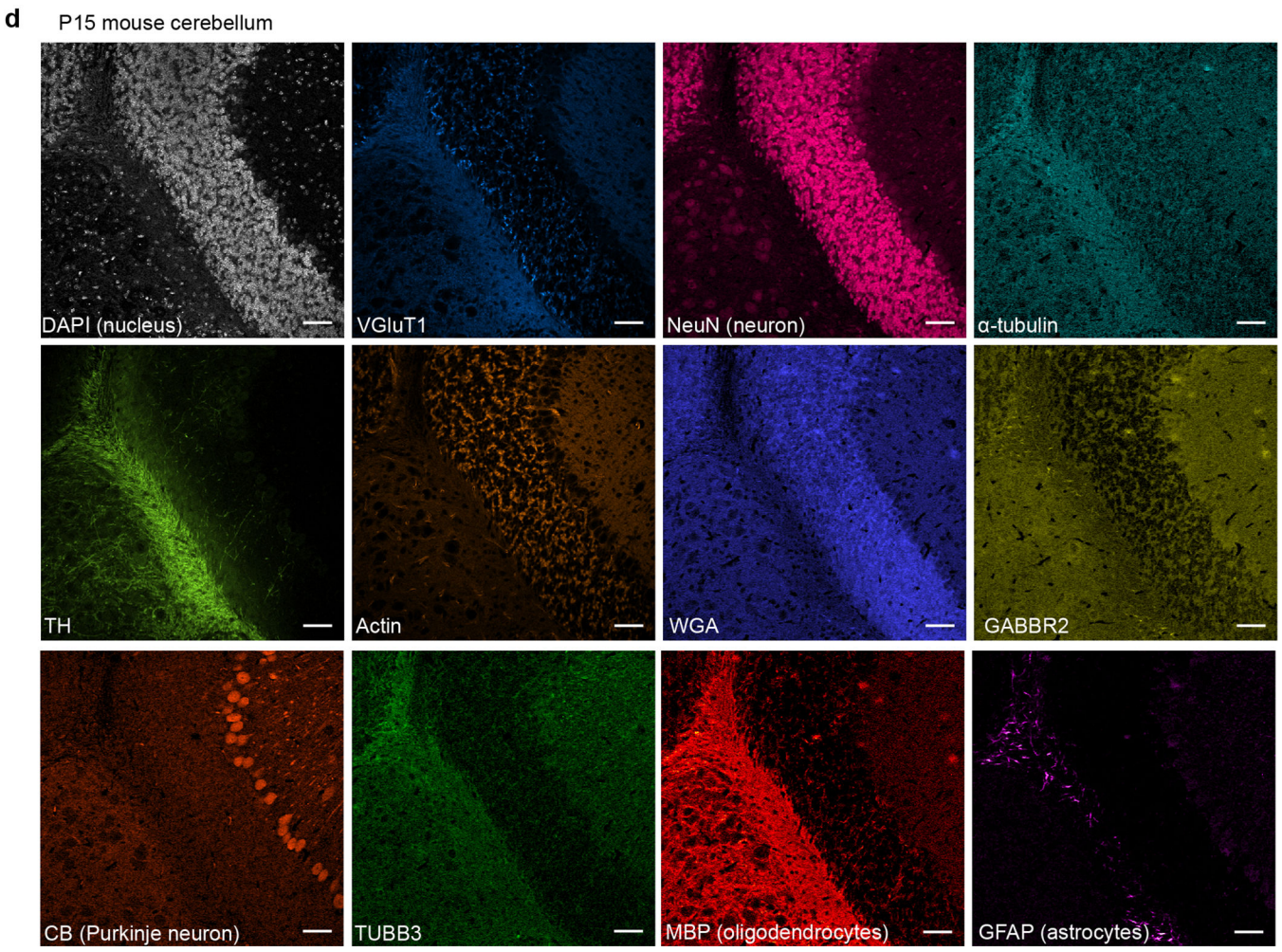

Extended Data Fig. 5. Simultaneous twelve-target imaging in mouse cerebellum thin sections

a, Two-color imaging tests on fixed cells (nucleus protein H2B labeled by O-cored MARS and cytoskeleton protein β-tubulin labeled by C-cored dyes). No obvious cross-talk between two channels was observed. (left) β-tubulin (labeled by MARS2176) and H2B (labeled by MARS2188). (right) β-tubulin (labeled by MARS2176) and H2B (labeled by MARS2242). **b**, A workflow of multiplexed labeling (also see methods). **c**, **d**, Simultaneous twelve-target protein imaging on cerebellum tissue sections from (**c**) postnatal 25 days (P25) and (**d**) postnatal 15 days (P15) mice. Fluorescence: DAPI (total DNA), vesicular glutamate transporter 1 (VGluT1-Alexa Fluor 488, Glutamatergic neurons, direct immunolabeling), tyrosine hydroxylase (TH-Alexa Fluor 594, Dopaminergic neurons, direct immunolabeling), actin (Phalloidin-Alexa Fluor 647); epr-SRS: neuronal nuclei (NeuN, neurons, MARS2228), α-tubulin-MARS2176 (direct immunolabeling), calbindin (CB, Purkinje neurons, MARS2145), β-III-tubulin (TUBB3, neurons, MARS2200), wheat germ agglutinin (WGA-MARS2242), GABA B receptor 2 (GABBR2, GABAergic neurons, MARS2212), myelin basic protein (MBP; oligodendrocytes, MARS2188), glial fibrillary acidic protein (GFAP, astrocytes and neural stem cells, MARS2159). Scale bars, 20 μm in (**a**); 50 μm in (**c–d**).

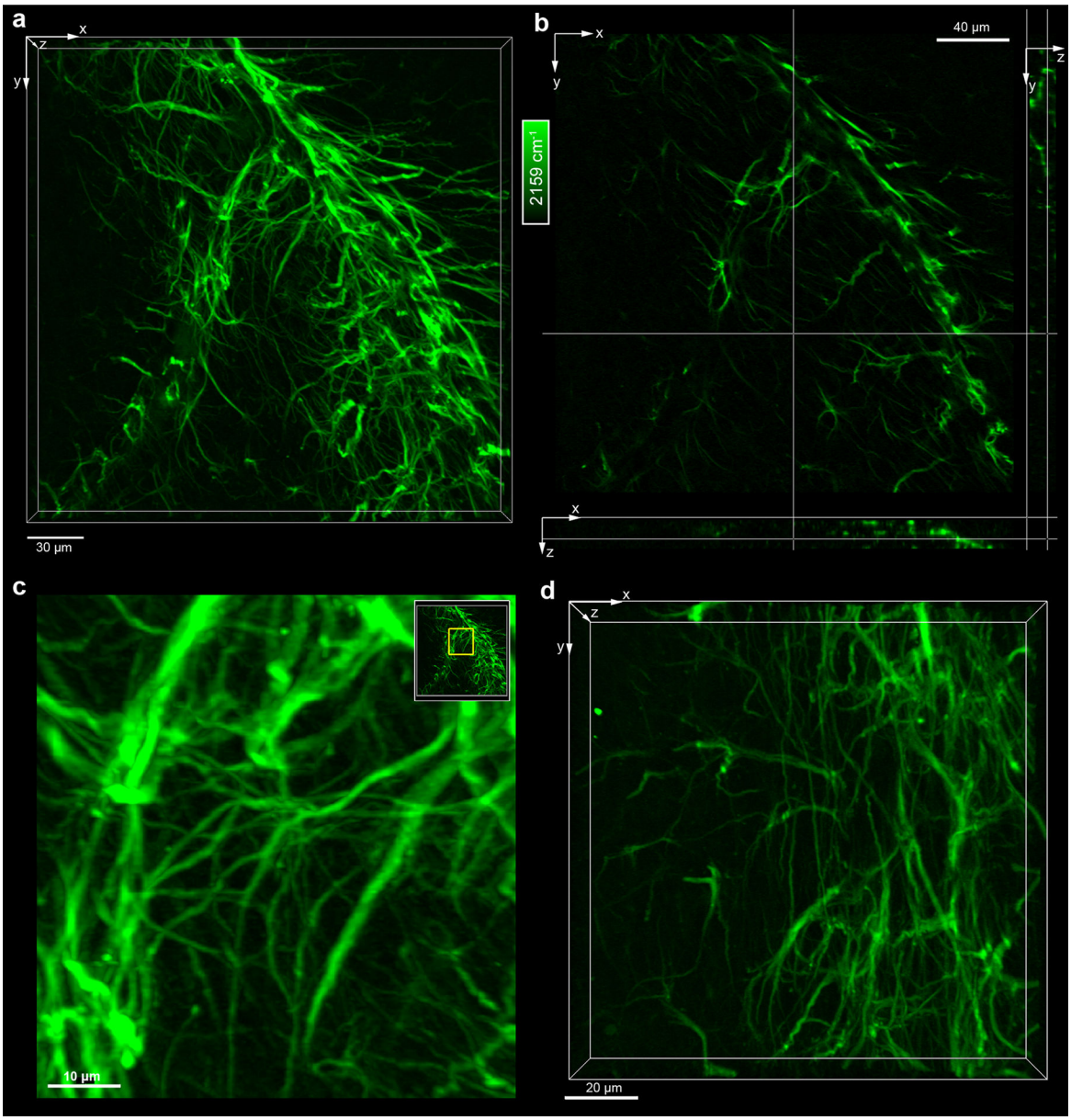

Extended Data Fig. 6. Sectioning capability and axial resolution of immuno-eprSRS imaging

a, Volume-rendered image; **b**, Orthogonal views; **c**, Zoomed-in volume-rendered image of (**a**); **d**, Optically zoomed-in volume-rendered image of MARS2159 stained GFAP in 100-μm thick mouse brain tissue. The inset yellow box in (**c**) represents the position of the enlarged region. Step size of z is 2 μm in (**a–c**) and is 1 μm in (**d**). Scale bars, 30 μm in (**a**); 40 μm in (**b**); 10 μm in (**c**); 20 μm in (**d**).

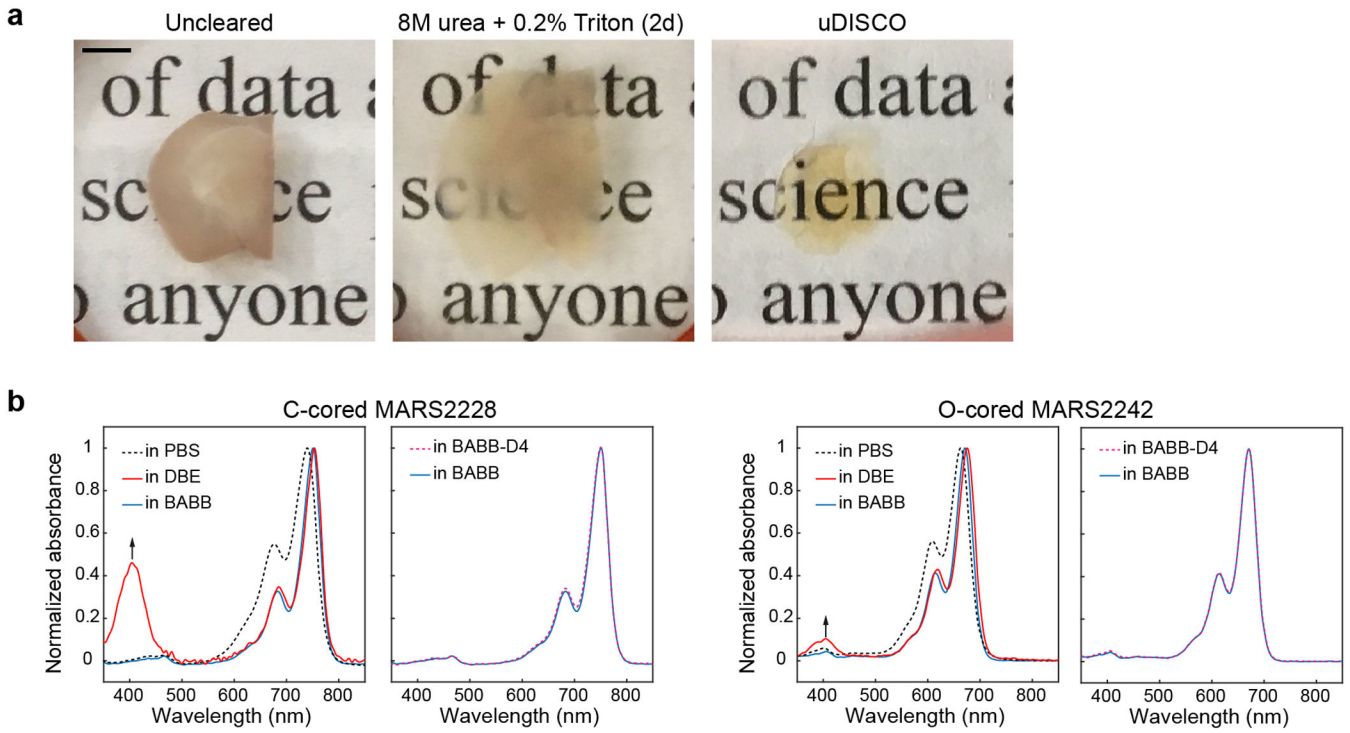

Extended Data Fig. 7. Tests on immuno-eprSRS for volumetric imaging

a, Photos of 1-mm thick brain slices without clearing (uncleared), cleared by 8 M urea and 0.2% Triton for 2 days and cleared by uDISCO. Scale bar, 2 mm. **b**, Normalized absorption spectra of MARS probes in RI matching solutions in BABB, 3DISCO (DBE) and uDISCO (BABB-D4). A bluer absorption peak appears in DBE, but not in BABB and BABB-D4.

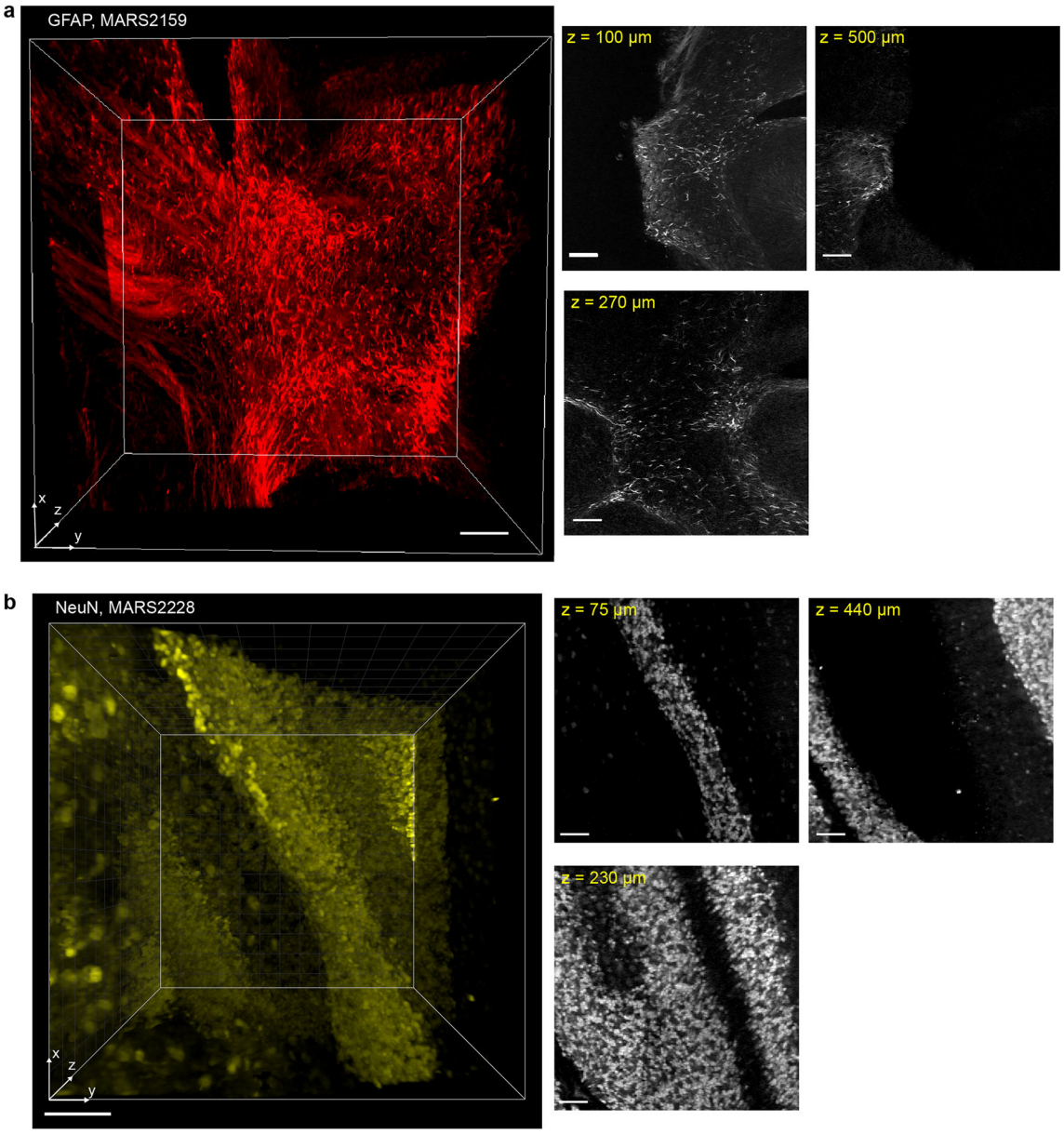

Extended Data Fig. 8. Volumetric immuno-eprSRS imaging on 500-μm-thick mouse cerebellum sections with uDISCO clearing

a, Volume-rendered image of GFAP (astrocytes) labeled with O-cored MARS2159 in 500-μm thick cerebellum sections cleared by uDISCO. **b**, Volume-rendered image of NeuN (neuronal nucleus) labeled with C-cored MARS2228 in 500-μm thick cerebellum sections cleared by uDISCO. Enlarged images of Fig. 4a. Single-plane images show good epr-SRS contrast along the whole depth for both samples. Scale bars, 100 μm.

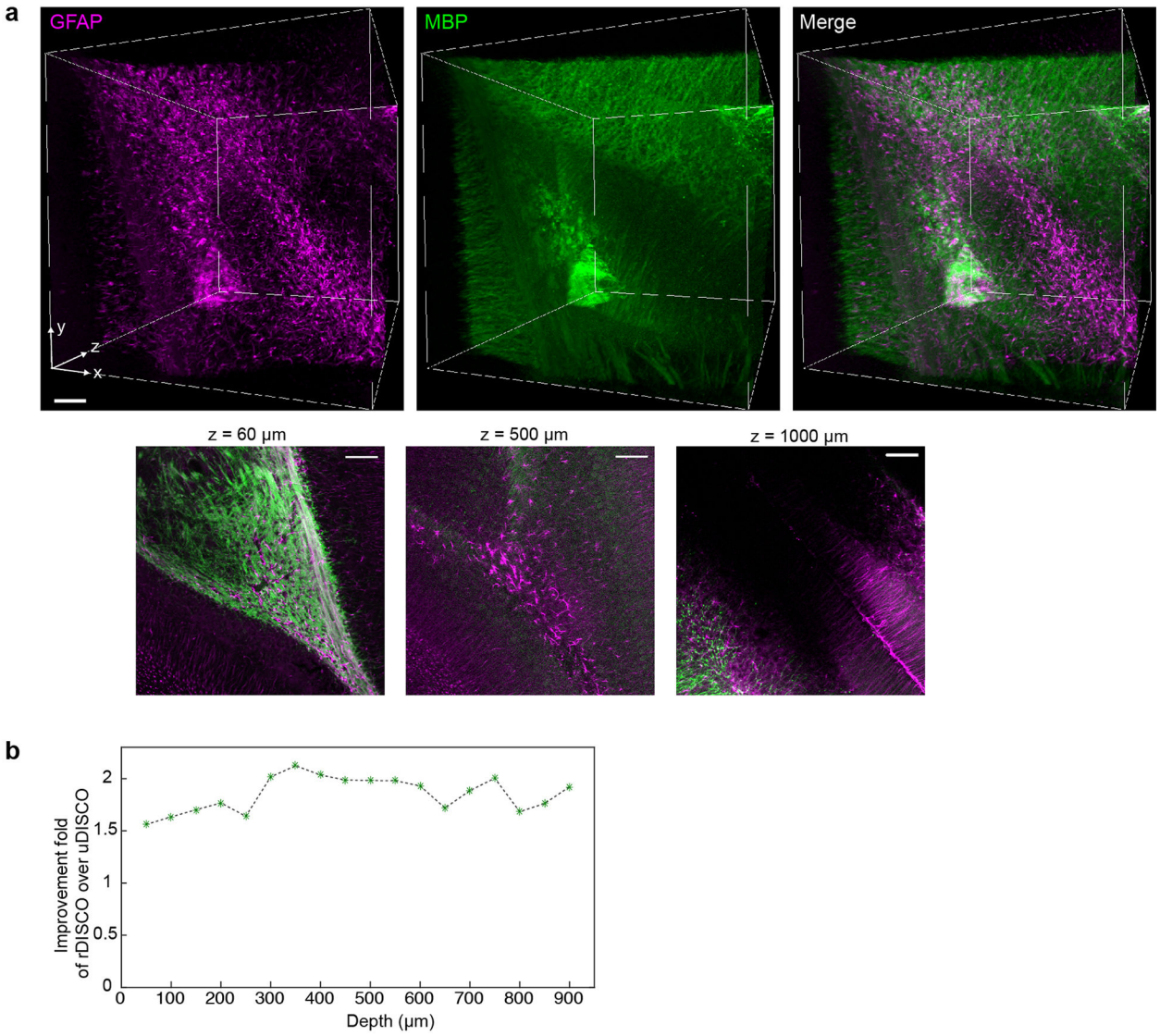

Extended Data Fig. 9. Improvement of rDISCO over uDISCO on volumetric immuno-eprSRS imaging

a, Volume-rendered images of GFAP (astrocytes, labeled with MARS2228) and MBP (oligodendrocytes, labeled with Alexa Fluor 488) in 1-mm thick cerebellum sections cleared by uDISCO. Two-color merged single-plane images also show good epr-SRS and fluorescence contrast along the whole depth. Scale bars, 100 μm. **b**, SRS signal-to-noise ratio improvement of rDISCO over uDISCO at different depths.

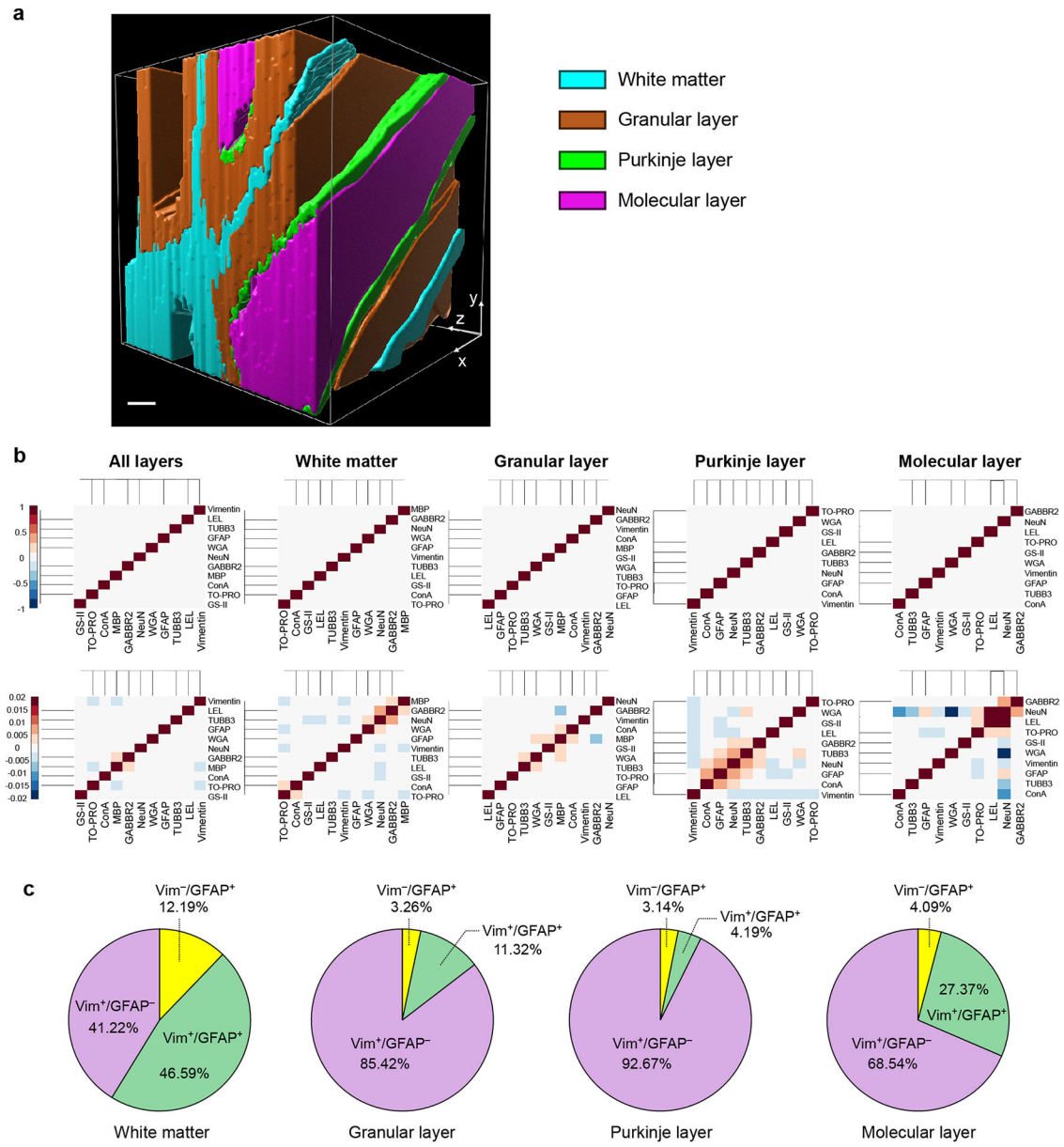

Extended Data Fig. 10. Quantitative 3D analyses on multiplexed volumetric images

a, Segmentation of four anatomical layers as white matter, the granular layer, the Purkinje layer and the molecular layer. Scale bar, 100 μm. **b**, Correlation heatmaps between randomized images. (up) Color bar plotted in the range of [−1 1]. (down) Color bar plotted in the range of [−0.02 0.02]. **c**, Compositional percentages of $Vim^+/GFAP^-$, $Vim^-/GFAP^+$ and $Vim^+/GFAP^+$ cells for four layers.

Supplementary Material

Refer to Web version on PubMed Central for supplementary material.

Acknowledgments

We thank Rafael Yuste, Raju Tomer, Lu Wei, Fanghao Hu and Chen Chen for helpful discussions. W.M. acknowledges support from NIH R01 (GM128214), R01 (GM132860) and R01 (EB029523).

Data availability

All data that support the findings of this study are available from the corresponding author upon reasonable request. Source data are provided with this paper.

Reference

1. Luo C et al. Single-cell methylomes identify neuronal subtypes and regulatory elements in mammalian cortex. Science 357, 600, (2017). [PubMed: 28798132]
2. Lichtman JW & Denk W The big and the small: challenges of imaging the brain's circuits. Science 334, 618, (2011). [PubMed: 22053041]
3. Tsurui H et al. Seven-color fluorescence imaging of tissue samples based on Fourier spectroscopy and singular value decomposition. J. Histochem. Cytochem 48, 653–662, (2000). [PubMed: 10769049]
4. Cutrale F et al. Hyperspectral phasor analysis enables multiplexed 5D in vivo imaging. Nat. Methods 14, 149–152, (2017). [PubMed: 28068315]
5. Angelo M et al. Multiplexed ion beam imaging of human breast tumors. Nat. Med 20, 436–442, (2014). [PubMed: 24584119]
6. Giesen C et al. Highly multiplexed imaging of tumor tissues with subcellular resolution by mass cytometry. Nat. Methods 11, 417–422, (2014). [PubMed: 24584193]
7. Gerdes MJ et al. Highly multiplexed single-cell analysis of formalin-fixed, paraffin-embedded cancer tissue. Proc. Nat. Acad. Sci. U.S.A 110, 11982, (2013).
8. Lin J-R et al. Highly multiplexed immunofluorescence imaging of human tissues and tumors using t-CyCIF and conventional optical microscopes. Elife 7, e31657, (2018). [PubMed: 29993362]
9. Gut G, Herrmann MD & Pelkmans L Multiplexed protein maps link subcellular organization to cellular states. Science 361, eaar7042, (2018). [PubMed: 30072512]
10. Goltsev Y et al. Deep profiling of mouse splenic architecture with CODEX multiplexed imaging. Cell 174, 968–981.e915, (2018). [PubMed: 30078711]
11. Chung K et al. Structural and molecular interrogation of intact biological systems. Nature 497, 332–337, (2013). [PubMed: 23575631]
12. Renier N et al. iDISCO: a simple, rapid method to immunolabel large tissue samples for volume imaging. Cell 159, 896–910, (2014). [PubMed: 25417164]
13. Murray E et al. Simple, scalable proteomic imaging for high-dimensional profiling of intact systems. Cell 163, 1500–1514, (2015). [PubMed: 26638076]
14. Ku T et al. Multiplexed and scalable super-resolution imaging of three-dimensional protein localization in size-adjustable tissues. Nat. Biotechnol 34, 973–981, (2016). [PubMed: 27454740]
15. Park Y-G et al. Protection of tissue physicochemical properties using polyfunctional crosslinkers. Nat. Biotechnol 37, 73–83, (2019).
16. Wei L et al. Super-multiplex vibrational imaging. Nature 544, 465–470, (2017). [PubMed: 28424513]
17. Kawata S, Ichimura T, Taguchi A & Kumamoto Y Nano-Raman scattering microscopy: resolution and enhancement. Chem. Rev 117, 4983–5001, (2017). [PubMed: 28337915]
18. Wei L & Min W Electronic preresonance stimulated Raman scattering microscopy. J. Phys. Chem. Lett 9, 4294–4301, (2018). [PubMed: 30001137]
19. Miao Y, Shi L, Hu F & Min W Probe design for super-multiplexed vibrational imaging. Phys. Biol 16, 041003, (2019). [PubMed: 30870829]
20. Richardson DS & Lichtman JW Clarifying tissue clearing. Cell 162, 246–257, (2015). [PubMed: 26186186]

21. Ueda HR et al. Tissue clearing and its applications in neuroscience. Nat. Rev. Neurosci 21, 61–79, (2020). [PubMed: 31896771]
22. Dougan JA & Faulds K Surface enhanced Raman scattering for multiplexed detection. Analyst 137, 545–554, (2012). [PubMed: 22186980]
23. Hama H et al. ScaleS: an optical clearing palette for biological imaging. Nat. Neurosci 18, 1518–1529, (2015). [PubMed: 26368944]
24. Zhu X et al. Ultrafast optical clearing method for three-dimensional imaging with cellular resolution. Proc. Nat. Acad. Sci. U.S.A 116, 11480, (2019).
25. Li W, Germain RN & Gerner MY Multiplex, quantitative cellular analysis in large tissue volumes with clearing-enhanced 3D microscopy (Ce3D). Proc. Nat. Acad. Sci. U.S.A 114, E7321, (2017).
26. Ertürk A et al. Three-dimensional imaging of solvent-cleared organs using 3DISCO. Nat. Protoc 7, 1983–1995, (2012). [PubMed: 23060243]
27. Pan C et al. Shrinkage-mediated imaging of entire organs and organisms using uDISCO. Nat. Methods 13, 859–867, (2016). [PubMed: 27548807]
28. Hu F, Shi L & Min W Biological imaging of chemical bonds by stimulated Raman scattering microscopy. Nat. Methods 16, 830–842, (2019). [PubMed: 31471618]
29. Wei M et al. Volumetric chemical imaging by clearing-enhanced stimulated Raman scattering microscopy. Proc. Nat. Acad. Sci. U.S.A 116, 6608, (2019).
30. Bata JE, Gyenes L & Sehon AH The effect of urea of antibody-antigen reactions. Immunochemistry 1, 289–293, (1964). [PubMed: 14250782]
31. Qi Y et al. FDISCO: Advanced solvent-based clearing method for imaging whole organs. Sci. Adv 5, eaau8355, (2019). [PubMed: 30746463]
32. Hahn C et al. High-resolution imaging of fluorescent whole mouse brains using stabilised organic media (sDISCO). J. Biophotonics 12, e201800368, (2019). [PubMed: 30932329]
33. Medina ME, Iuga C & Alvarez-Idaboy JR Antioxidant activity of propyl gallate in aqueous and lipid media: a theoretical study. Phys. Chem. Chem. Phys 15, 13137–13146, (2013). [PubMed: 23824251]
34. Haseloff RF, Blasig IE, Meffert H & Ebert B Hydroxyl radical scavenging and antipsoriatic activity of benzoic acid derivatives. Free Radic. Biol. Med 9, 111–115, (1990). [PubMed: 2172097]
35. LlinÁS RR, Walton KD & Lang EJ “Ch. 7 Cerebellum” In The Synaptic Organization of the Brain. (Oxford University Press., 2004).
36. Katsetos CD, Herman MM & Mörk SJ Class III β-tubulin in human development and cancer. Cell Motil. Cytoskeleton 55, 77–96, (2003). [PubMed: 12740870]
37. Schnitzer J, Franke WW & Schachner M Immunocytochemical demonstration of vimentin in astrocytes and ependymal cells of developing and adult mouse nervous system. J. Cell Biol 90, 435–447, (1981). [PubMed: 7026573]
38. Bovolenta P, Liem RKH & Mason CA Development of cerebellar astroglia: Transitions in form and cytoskeletal content. Dev. Biol 102, 248–259, (1984). [PubMed: 6538151]
39. Molofsky AV et al. Astrocytes and disease: a neurodevelopmental perspective. Genes Dev. 26, 891–907, (2012). [PubMed: 22549954]
40. McCaslin AFH, Chen BR, Radosevich AJ, Cauli B & Hillman EMC In vivo 3D morphology of astrocyte—vasculature interactions in the somatosensory cortex: implications for neurovascular coupling. J. Cereb. Blood Flow Metab 31, 795–806, (2010). [PubMed: 21139630]
41. Zerlin M & Goldman JE Interactions between glial progenitors and blood vessels during early postnatal corticogenesis: Blood vessel contact represents an early stage of astrocyte differentiation. J. Comp. Neurol 387, 537–546, (1997). [PubMed: 9373012]
42. Paredes I, Himmels P & Ruiz de Almodóvar C Neurovascular communication during CNS development. Dev. Cell 45, 10–32, (2018). [PubMed: 29634931]
43. Liedtke W et al. GFAP is necessary for the integrity of CNS white matter architecture and long-term maintenance of myelination. Neuron 17, 607–615, (1996). [PubMed: 8893019]
44. Ishibashi T et al. Astrocytes promote myelination in response to electrical impulses. Neuron 49, 823–832, (2006). [PubMed: 16543131]

45. Lundgaard I, Osório MJ, Kress BT, Sanggaard S & Nedergaard M White matter astrocytes in health and disease. Neurosci. 276, 161–173, (2014).
46. Barabási A-L & Oltvai ZN Network biology: understanding the cell's functional organization. Nat. Rev. Genet 5, 101–113, (2004). [PubMed: 14735121]
47. Albert R Scale-free networks in cell biology. J. Cell Sci 118, 4947, (2005). [PubMed: 16254242]
48. Jeong H, Mason SP, Barabási AL & Oltvai ZN Lethality and centrality in protein networks. Nature 411, 41–42, (2001). [PubMed: 11333967]
49. Abbott NJ, Rönnbäck L & Hansson E Astrocyte–endothelial interactions at the blood–brain barrier. Nat. Rev. Neurosci 7, 41–53, (2006). [PubMed: 16371949]
50. Freeman Marc R. & Rowitch David H. Evolving concepts of gliogenesis: A look way back and ahead to the next 25 years. Neuron 80, 613–623, (2013). [PubMed: 24183014]
51. Gulati AK, Zalewski AA, Sharma KB, Ogrowsky D & Sohal GS A comparison of lectin binding in rat and human peripheral nerve. J. Histochem. Cytochem 34, 1487–1493, (1986). [PubMed: 3772078]
52. Bettler B, Kaupmann K, Mosbacher J & Gassmann M Molecular structure and physiological functions of GABAB receptors. Physiol. Rev 84, 835–867, (2004). [PubMed: 15269338]
53. Burgoyne RD, Cambray-Deakin MA, Lewis SA, Sarkar S & Cowan NJ Differential distribution of beta-tubulin isotypes in cerebellum. EMBO J. 7, 2311–2319, (1988). [PubMed: 2461292]
54. Tischfield MA et al. Human TUBB3 mutations perturb microtubule dynamics, kinesin interactions, and axon guidance. Cell 140, 74–87, (2010). [PubMed: 20074521]
55. Yun DH et al. Ultrafast immunostaining of organ-scale tissues for scalable proteomic phenotyping. bioRxiv, 660373, (2019).
56. Saka SK et al. Immuno-SABER enables highly multiplexed and amplified protein imaging in tissues. Nat. Biotechnol 37, 1080–1090, (2019). [PubMed: 31427819]
57. Lin R et al. A hybridization-chain-reaction-based method for amplifying immunosignals. Nat. Methods 15, 275–278, (2018). [PubMed: 29481551]
58. Hu F et al. Supermultiplexed optical imaging and barcoding with engineered polyynes. Nat. Methods 15, 194–200, (2018). [PubMed: 29334378]
59. Biot E et al. in 2008 5th IEEE International Symposium on Biomedical Imaging: From Nano to Macro. 975–978.
60. Tun K Graph package (https://www.mathworks.com/matlabcentral/fileexchange/12648-graph-package). MATLAB Central File Exchange. Retrieved May 5, 2021.

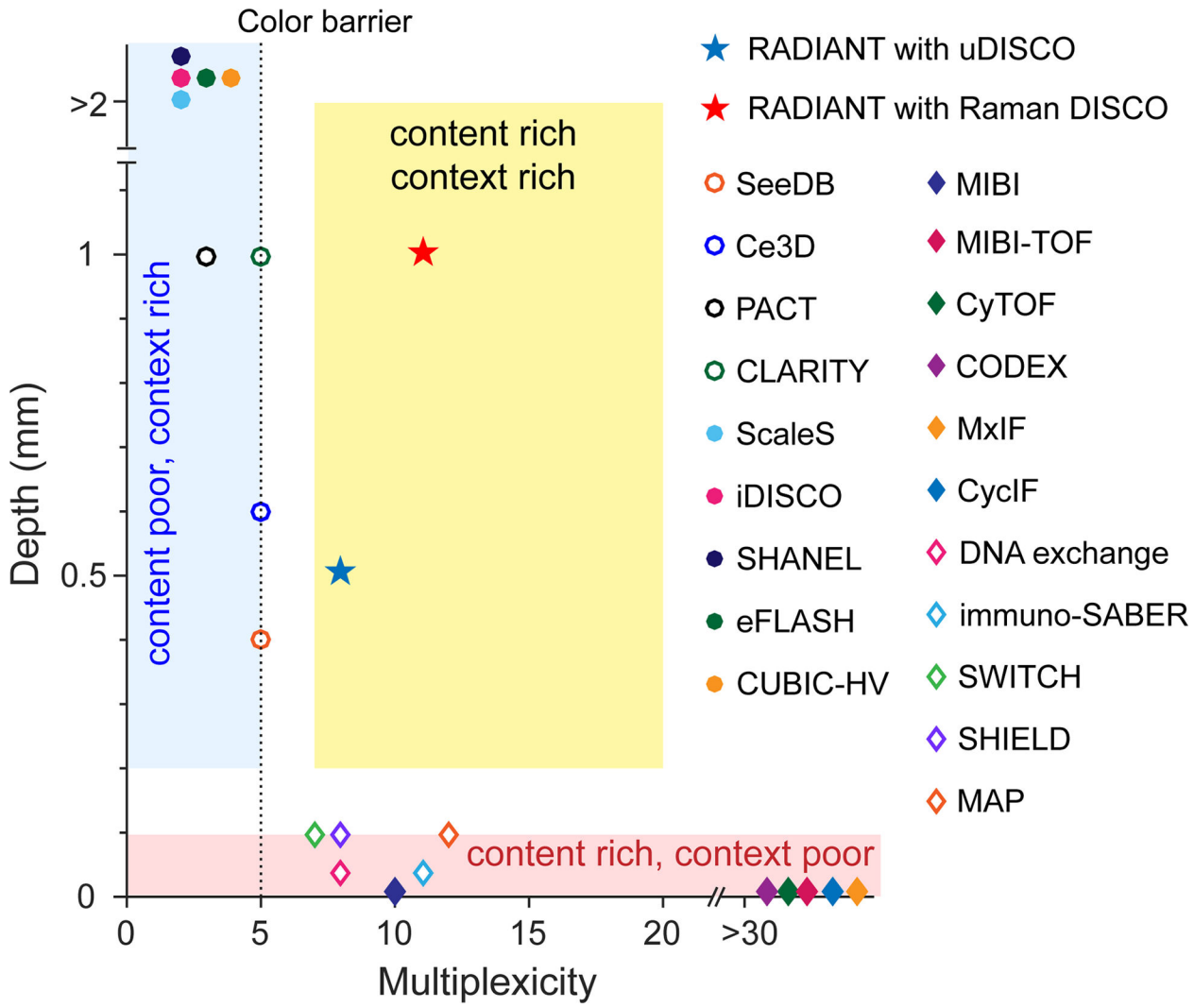

Fig.1. The limitations of existing protein imaging methods towards highly multiplexed volumetric protein imaging.

A summary about the details of listed methods can be found in Supplementary Table 1. Color barrier: typically, no more than five colors can be detected simultaneously by fluorescence microscopy. A general trade-off between content (high multiplexity) and context (thick samples) restricts the use of existing protein imaging methods towards highly multiplexed volumetric protein imaging. RADIANT breaks the content-context trade-off (yellow region).

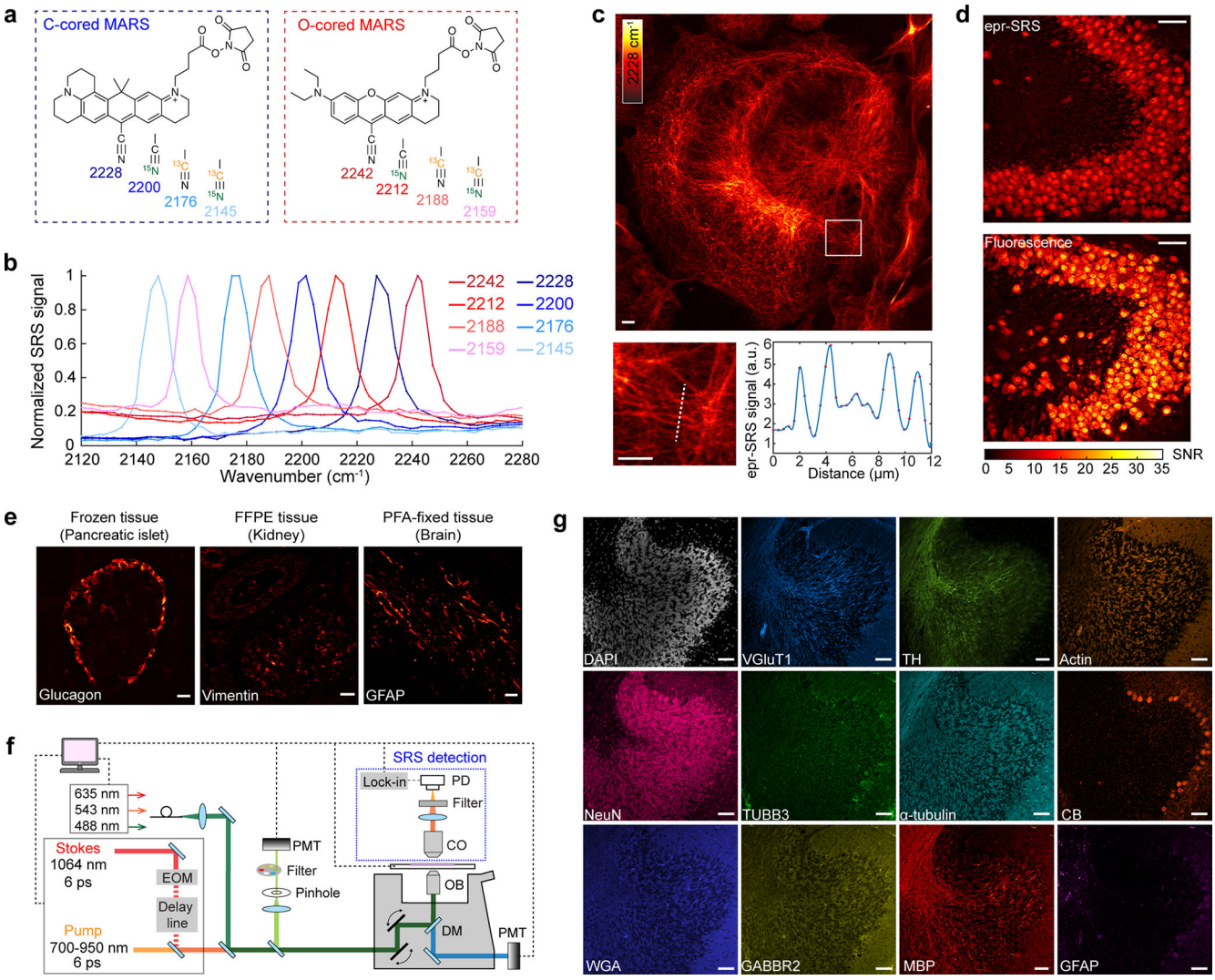

Fig. 2. Selection and expansion of MARS palette for one-shot multiplexed protein imaging.

a, Structures of C-cored and O-cored NHS-ester-functionalized MARS probes, each with four isotope combinations on the nitrile bond. **b**, epr-SRS spectra of the selected eight NHS-ester-functionalized MARS probes. **c**, Diffraction-limited immuno-eprSRS imaging of α-tubulin. **d**, Comparison of immuno-eprSRS with conventional immunofluorescence using the same primary antibody. **e**, Immuno-eprSRS is compatible with common tissue preparations: frozen tissue of mouse pancreas with Glucagon labelled by MARS2176; formalin-fixed paraffin-embedded (FFPE) tissue of human kidney with Vimentin labelled by MARS2200; PFA-fixed mouse brain tissue with GFAP labelled by MARS2145. **f**, A multi-modality platform of SRS-fluorescence tandem imaging. EOM, electro-optics modulator; DM, dichromic mirror; OB, objective; CO, condenser; PD, photodiode; PMT, photomultiplier tube. **g**, Simultaneous twelve-target imaging on mouse cerebellum thin section. Fluorescence: DAPI (DNA), vesicular glutamate transporter 1 (VGluT1-Alexa Fluor 488, Glutamatergic neurons, direct immunolabeling), tyrosine hydroxylase (TH-Alexa Fluor 594, Dopaminergic neurons, direct immunolabeling), F-actin (Phalloidin-Alexa Fluor 647); epr-SRS: neuronal nuclei (NeuN, neurons, MARS2228), α-tubulin-MARS2176

(direct immunolabeling), calbindin (CB, Purkinje neurons, MARS2145), β-III-tubulin (TUBB3, neurons, MARS2200), wheat germ agglutinin (WGA-MARS2242), GABA B receptor 2 (GABBR2, GABAergic neurons, MARS2212), myelin basic protein (MBP; oligodendrocytes, MARS2188), glial fibrillary acidic protein (GFAP, astrocytes and neural stem cells, MARS2159). Antibody information can be found in Supplementary Table 3. Scale bars, 10 μm in (**c**); 50 μm in (**d–e**, **g**).

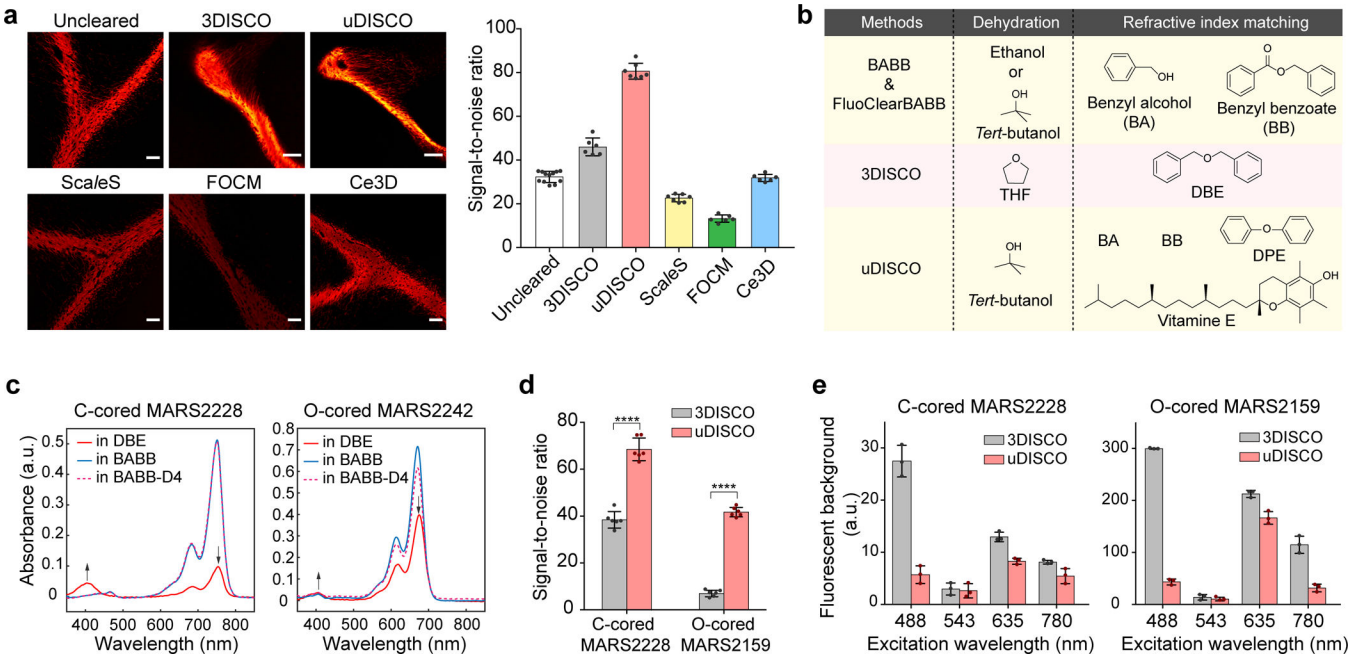

Fig. 3. Screening and studying tissue clearing protocols for immuno-eprSRS of MARS probes.

a, Screening tissue clearing protocols for immuno-eprSRS. Left, representative epr-SRS images of MBP (labeled with MARS2176) in cerebellum tissues (40-μm thick) cleared by each protocol. Scale bars, 50 μm. Right, quantification of epr-SRS signal-to-noise ratios for different clearing methods (n=12, 6, 7, 7, 6, 6 regions of interest (ROIs)). **b**, Chemicals used for dehydration and refractive index matching in BABB/FluoClearBABB, 3DISCO and uDISCO. uDISCO utilizes a mixture of BA, BB and DPE (called BABB-D4) supplemented with vitamin E for refractive index matching. **c**, Absorption spectra of MARS probes freshly dissolved in DBE, BABB and BABB-D4 solutions. Arrows indicate a substantial intensity decrease in DBE compared to either BABB or BABB-D4, and the increase of a bluer absorption band. **d**, Comparison of epr-SRS signal-to-noise ratios between 3DISCO and uDISCO (n=6 ROIs). 100-μm thick cerebellum tissues with GFAP labeled by MARS2228 or MARS2159 were used. Two-tailed unpaired *t*-test, left: $P=2.2\times10^{-7}$, $t=12$; right: $P=8.8\times10^{-12}$, $t=35$. **e**, Comparison of post-clearing fluorescence background between 3DISCO and uDISCO (n=3 ROIs). Same samples were used as in (**d**). 780 nm excitation represents two-photon fluorescence channel excited by 780-nm pump laser. All data in Fig.3 are presented as mean ± s.d..

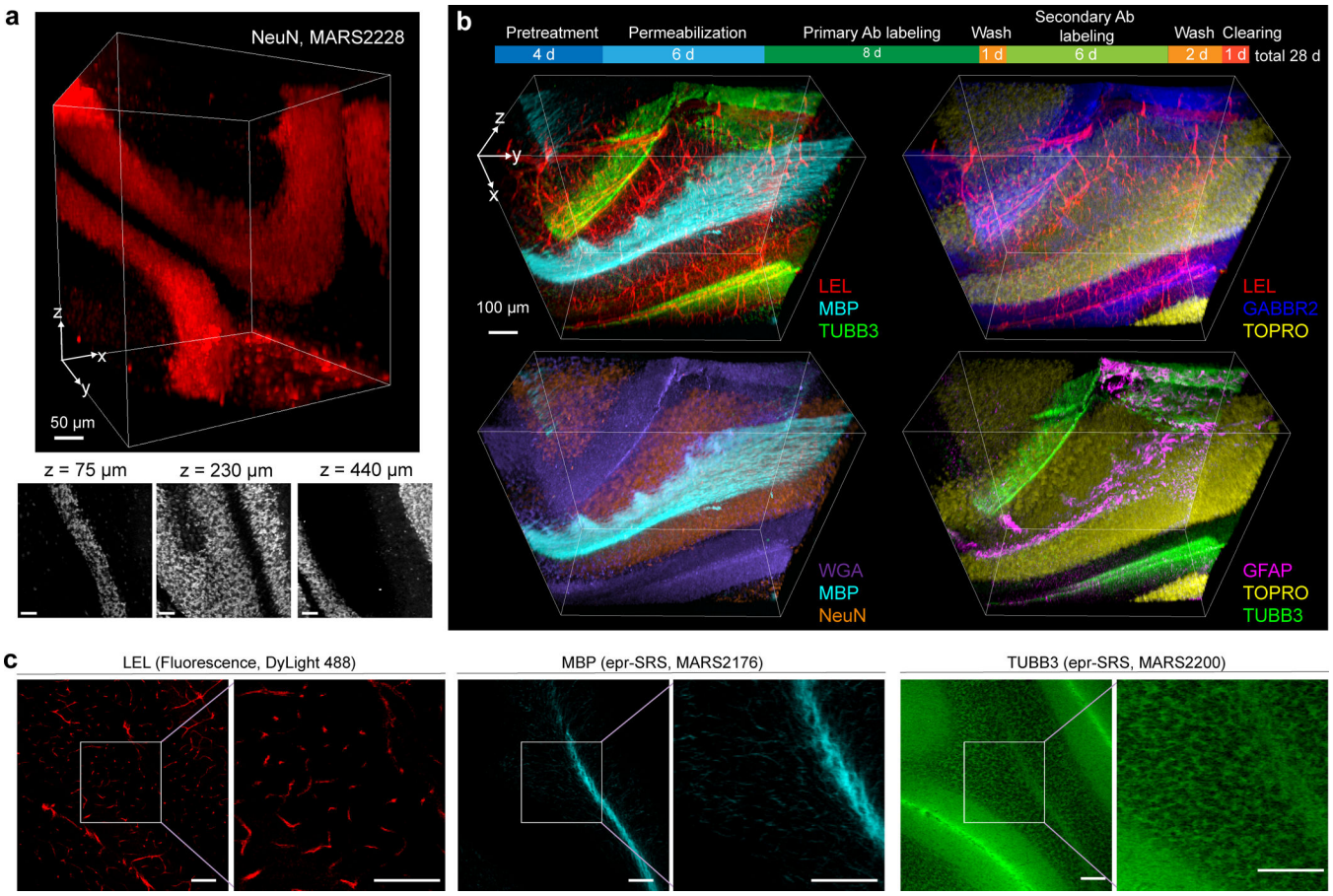

Fig. 4. Volumetric immuno-eprSRS imaging with uDISCO clearing.

a, 3D reconstruction of NeuN (granular neurons) labeled with C-cored MARS2228 in 500-μm thick cerebellum sections cleared by uDISCO. 2D images show good epr-SRS contrast along the whole depth. Scale bars, 50 μm. **b**, One-shot eight-target volume-rendered images of a 500-μm thick mouse cerebellum section by RADIANT. A typical workflow for tissue sample preparation, staining and clearing is depicted. Ab, antibody. Fluorescence: LEL (*Lycopersicon Esculentum* lectin DyLight 488), TO-PRO-3 (cell nucleus stain); epr-SRS: NeuN (MARS2228), TUBB3 (MARS2200), MBP (MARS2176), GABBR2 (MARS2145), WGA (MARS2242), GFAP (MARS2159). **c**, Representative single-plane images with zoom-in images at z = 250 μm of 3D data set in (**b**). Scale bars, 100 μm.

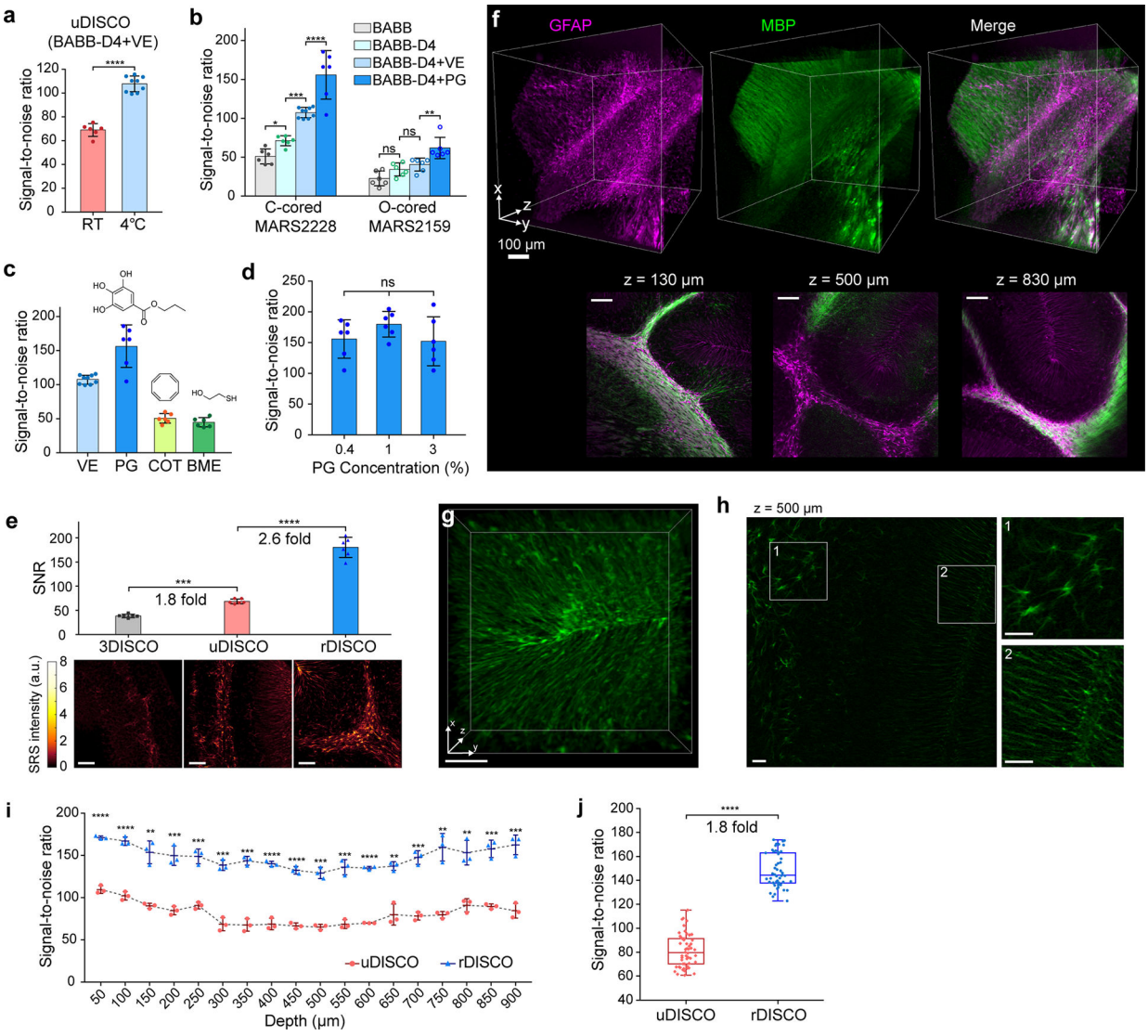

Fig. 5. Development of MARS-probe tailored Raman DISCO (rDISCO) with improved performance.

a, Temperature study with uDISCO. Two-tailed unpaired *t*-test (n=6, 9 ROIs), P=2.3×10^{-8}, t=12. **b–d**, Screening strategies to further scavenge peroxides for better MARS probe preservation. **b**, One-way ANOVA followed by Holm-Bonferroni's *post hoc* test, (left panel) n=6, 6, 9, 6 ROIs, P=0.039, 2.7×10^{-4}, 7.8×10^{-6}; (right panel) n=5 ROIs, P=0.066, 0.31 and 1.6×10^{-3}. **d**, One-way ANOVA test (n=6 ROIs), P = 0.29. In (**a–c**), VE: Vitamin E, PG: propyl gallate, COT: 1,3,5,7-cyclooctatetraene, BME: β-mercaptoethanol; 0.4% VE, PG, COT and BME were added. **e**, Comparison of epr-SRS signal-to-noise ratio among 3DISCO, uDISCO and rDISCO. One-way ANOVA followed by Holm-Bonferroni *post hoc* test (n=6 ROIs), P=7.9×10^{-4} and 1.3×10^{-10}. Representative images for three methods were shown below the bar graph. 100-μm thick mouse cerebellum tissue samples with GFAP labeled by MARS2228 or MARS2159 were used in (**a–e**). MARS2228 was used in (**a**, **c–e**). In (**b–d**), clearing was performed under 4 °C. **f**, Volume-rendered images of GFAP (astrocytes, labeled with MARS2145) and MBP (oligodendrocytes, labeled with Alexa Fluor 488) in 1-mm thick

cerebellum sections cleared by rDISCO. Two-color merged single-plane images show good epr-SRS and fluorescence contrast along the whole depth. **g**, Zoomed-in, volume-rendered images GFAP (labeled with MARS2145) in 1-mm thick cerebellum section cleared by rDISCO. **h**, Single-plane images of (**g**) at 500-μm depth show fine spatial resolution to resolve fibral structures of astrocytes. Left, zoom into the regions outlined by the dashed white box. **i**, Comparison of epr-SRS signal-to-noise ratios between rDISCO and uDISCO over entire thickness of 1-mm thick samples (n=3 ROIs). Two-tailed unpaired *t*-test, all $P<0.0001$. **j**, Comparison of SRS signal-to-noise ratio (mean ± s.d.) between uDISCO and rDISCO among all selected depths (n=18 depths). Two-tailed paired *t*-test, $P=3.2\times10^{-19}$, $t=28$, mean of ratios on rDISCO/uDISCO is 1.85. All data in Fig. 5 are presented as mean ± s.d.. Scale bars, 50 μm in (**e**, **g–h**); 100 μm in (**f**).

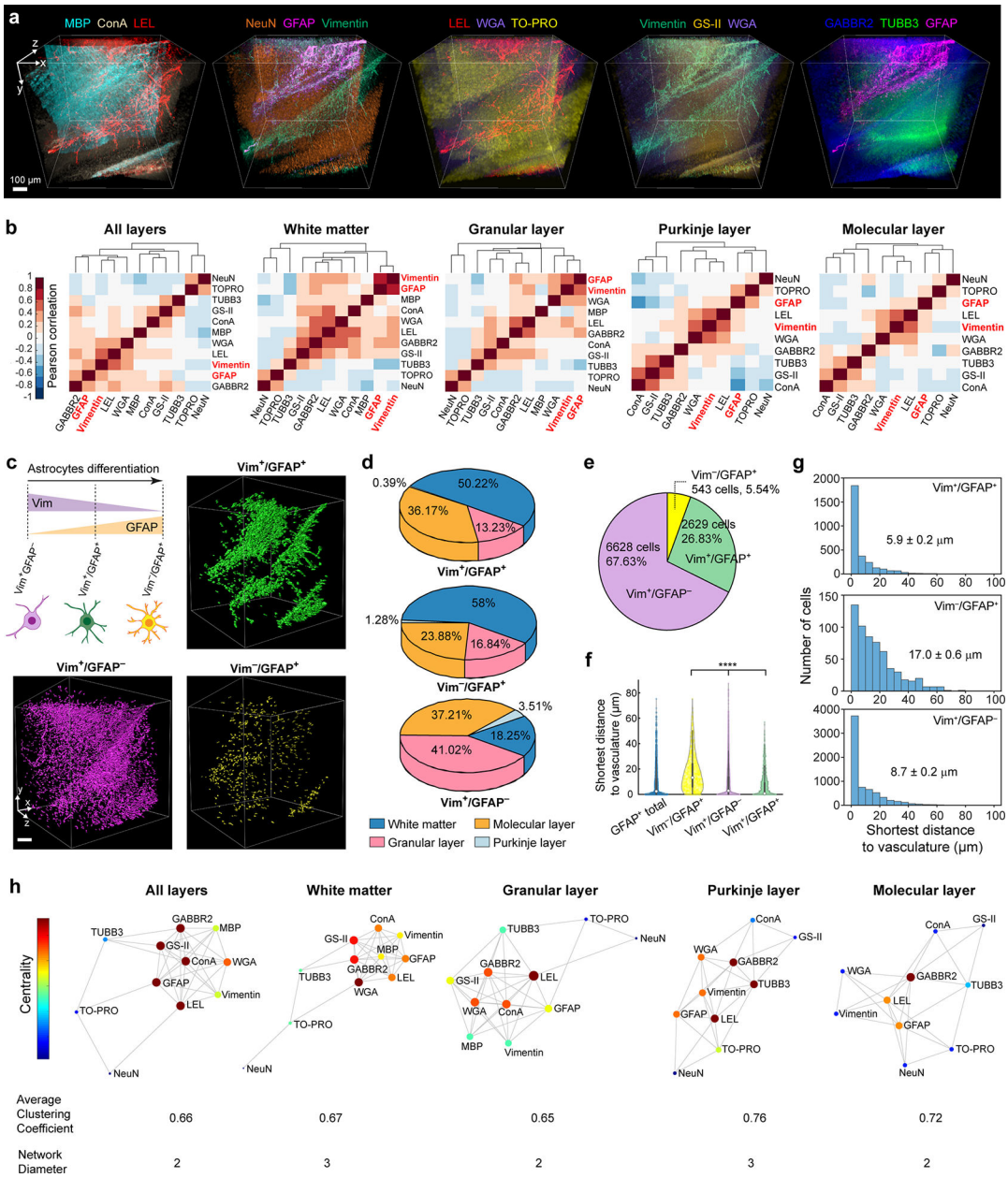

Fig. 6. RADIANT with rDISCO clearing enables millimeter-scale, highly-multiplexed protein imaging.

a, Eleven-target volume-rendered images of a 1-mm thick mouse cerebellum section by RADIANT with rDISCO clearing. Fluorescence: ConA (Concanavalin A, Alexa Fluor 350), GS-II (*Griffonia simplicifolia* lectin, Alexa Fluor 488), TUBB3 (Alexa Fluor 594, direct immunolabeling), TO-PRO-3 (cell nucleus stain); epr-SRS: NeuN (MARS2228), LEL (MARS2200), MBP (MARS2176), GABBR2 (MARS2145), WGA (MARS2242), Vimentin (MARS2212), GFAP (MARS2159). **b**, Pixel-based correlation heat maps for different regions of cerebellum. **c**, Segmentation of $Vim^+/GFAP^-$, $Vim^-/GFAP^+$ and $Vim^+/GFAP^+$ cells. The scheme shows the transition between three populations during astrocytes differentiation. **d**, Pie charts for cell compositional analysis of three populations in different

regions of cerebellum. **e**, Pie charts for the proportion of the three populations of cells. **f**, Violin plot of cell-to-nearest vasculature distances. One-way ANOVA followed by Holm-Bonferroni's *post hoc* tests were significant (n=3172, 543, 6625 and 2629 cells from a single mouse, $P<0.0001$). **g**, Histograms of cell-to-nearest vasculature distances of three populations of cells. Averaged distances (mean ± s.e.m) were shown inside graph. **h**, Network graph of correlations for different regions of cerebellum. Centrality is color-coded for each node. The node size is directly proportional to the numbers of edges connected to each node. Scale bars, 100 μm.